Advances in Science and Technology Research Journal

Advances in Science and Technology Research Journal, 2026, 20(10), 364–390
https://doi.org/10.12913/22998624/225641
ISSN 2299-8624, License CC-BY 4.0

Received: 2026.06.01
Accepted: 2026.07.19
Published: 2026.09.01

Influence of solid solution temperature in T6 heat treatment on the mechanical and corrosion characteristics of charge welded aluminum AA6061 hollow panels

Ericha D.W.S. Putri[1], Rama Gunawan[1], Yohanes P. D. S. Depari[2], Nurul Muhayat[1], Aditya Rio Prabowo[1], Triyono[1*]

[1] Mechanical Engineering Department, Universitas Sebelas Maret, Surakarta, Indonesia
[2] National Research and Innovation Agency of Republic Indonesia (BRIN), Jakarta Pusat, 10340, Indonesia
* Corresponding author's e-mail: triyono74@staff.uns.ac.id

ABSTRACT

The T6 heat treatment of aluminum extrusion profiles containing charge weld zones presents unique challenges, as solution temperature governs both the solute dissolution efficiency and the thermal stability of the weld interface. This study systematically investigates the influence of solid solution temperature (500 °C, 530 °C, and 560 °C, each for 6 h) within a T6 cycle on the mechanical properties, microstructural evolution, and electrochemical corrosion behavior of extruded AA6061 hollow panels, considering both panels without and with charge weld joints. Macrostructural and microstructural analyses, Vickers hardness profiling, uniaxial tensile testing, three-point bending, and potentiodynamic polarization tests in 3.5 wt.% NaCl solution were performed on skin and fin regions of all specimen groups. Solution treatment at 560 °C induced severe blistering and surface cracking attributed to entrapped hydrogen expansion under diminished hot strength, rendering those specimens structurally compromised. A solution temperature of 500 °C was identified as optimal, yielding the most favorable combination of grain refinement, precipitate homogeneity, hardness, tensile strength, and corrosion resistance in base-material panels. Relative to the as-extruded condition, T6 treatment at 500 °C increased Vickers hardness from 90–91 HVN to131–136 HVN, ultimate tensile strength from 303–318 MPa to 378–440 MPa, bending strength from 238–421 MPa to 318-489 MPa, and reduced the corrosion rate from 0.037–0.10 mm/y to 0.009–0.019 mm/y. Application of the T500 condition to charge-welded panels demonstrated that T6 heat treatment substantially recovered weld-zone hardness and tensile performance toward base-material levels, while also improving corrosion resistance relative to the as-extruded weld condition. Tensile strength of the weld region increased from 266–283 MPa to 380-387 MPa, bending strength from 127.5–276 MPa to 176–370 MPa, and corrosion rate decreased from 0.54–0.77 mm/y to 0.37–0.66 mm/y. These findings establish quantitative process-structure-property relationships for T6-treated AA6061 hollow extrusion panels and provide practical guidance for optimizing solution treatment parameters in lightweight structural applications that incorporate charge weld joints.

Keywords: AA6061 aluminum alloy, solid solution temperature, extrusion hollow panel, charge weld, corrosion resistance.

INTRODUCTION

Aluminum alloys of the 6xxx series have become indispensable in transportation, construction, and aerospace applications, where their combination of low density, corrosion resistance, and precipitation-hardenable strength addresses stringent structural and regulatory demands [1,2]. AA6061, in particular, stands as one of the most widely deployed alloys in this family, distinguished by its balanced strength-to-weight ratio, weldability, and compatibility with complex

forming processes [3]. The growing imperative for lightweighting in structural engineering has further elevated the relevance of aluminum extruded hollow panels, geometries that offer exceptional stiffness-to-weight efficiency and are increasingly specified for load-bearing applications in place of conventional solid sections [4].

A critical yet often overlooked aspect of hollow panel production is the practical constraint imposed by billet length and extrusion chamber capacity. In industrial practice, the maximum length of an extruded hollow panel is inherently limited by the volume of the billet and the physical length of the extrusion container. When structural applications demand panels exceeding these dimensional limits, as is frequently the case in transportation flooring, building façades, and bridge decking, panels must be produced by joining shorter extrusion segments end-to-end. Conventional fusion welding methods, however, are generally unsuitable for thin-walled hollow profiles due to risks of thermal distortion, porosity, and loss of base-metal properties in the heat-affected zone. Extrusion welding, also referred to as solid-state lap or butt joining of extruded profiles, offers a viable alternative for extending panel length while preserving structural integrity. In this process, two extruded panel segments are joined through the application of pressure and localized deformation, enabling material continuity without the introduction of a fusion weld zone. The absence of bulk melting minimizes the formation of solidification defects, preserves the wrought microstructure, and retains more of the base-metal mechanical properties compared to conventional arc or MIG welding [5,6]. Nevertheless, the extrusion weld zone constitutes a metallurgically distinct region, characterized by disrupted grain morphology, potential oxide entrapment at the bond interface, and altered precipitate distributions, that may respond differently to subsequent heat treatment than the surrounding base material [7].

The mechanical performance of AA6061 is intrinsically linked to precipitation hardening realized through T6 heat treatment, a three-stage sequence comprising solution heat treatment, quenching, and artificial aging [8]. During the solution stage, Mg and Si are taken into supersaturated solid solution, establishing the solute reservoir from which metastable strengthening precipitates, principally the β″ and β′ phases, subsequently nucleate and grow during aging [9,10]. The completeness and homogeneity of solute dissolution at the solution stage are therefore decisive in determining the final precipitate density and distribution, and by extension, the achievable strength.

Among the controllable process parameters in T6 treatment, the solid solution temperature exerts a disproportionate influence on outcomes. Sub-optimal temperatures leave residual Mg_2Si undissolved, diminishing the solute available for precipitation hardening and yielding inferior tensile and hardness properties [11]. At the other extreme, excessive temperatures promote grain coarsening, incipient boundary melting, and dimensional distortion, risks that are magnified in thin-walled hollow extrusion profiles, where non-uniform thermal gradients and restricted section thicknesses create conditions fundamentally different from those in bulk or simple geometries [12]. In hollow panels containing extrusion weld zones, these thermal effects are compounded by the microstructural heterogeneity inherent to the weld region, raising further uncertainty about the appropriateness of heat treatment parameters derived from homogeneous base-material studies.

Despite a substantial body of literature on T6 heat treatment of AA6061 [13,14], systematic investigations targeting extruded hollow profiles, and in particular those containing extrusion weld joints, remain sparse. Most prior work has been conducted on bulk specimens or solid sections, leaving the interplay between solution temperature, microstructural evolution, and mechanical response in hollow extrusions, including their weld zones, inadequately characterized. The mechanistic linkages between temperature-driven changes in grain morphology, precipitate distribution, and the resulting tensile and hardness properties of welded hollow panel structures have not been rigorously established. This knowledge gap presents a practical obstacle to the rational design of heat treatment schedules for long-span, next-generation lightweight aluminum structures that inevitably incorporate extrusion weld joints.

To address this deficiency, the present study systematically investigates the effect of solid solution temperature on the mechanical and microstructural characteristics of AA6061 aluminum extruded hollow panels containing charge welds, subjected to T6 heat treatment. Tensile properties, hardness, grain morphology, precipitate distribution, and corrosion behavior are characterized across a range of solution temperatures, and the resulting process-structure-property relationships are analyzed in depth, with particular attention to

the response of the extrusion weld zone relative to the base material. The outcomes are intended to provide a mechanistic basis for optimizing solution heat treatment parameters and to serve as quantitative design guidance for practitioners developing high-performance, long-length aluminum hollow extrusion components.

MATERIALS AND METHODS

Material

The material used in this study was AA6061 aluminum alloy in the form of cylindrical billets. The nominal chemical composition conformed to the AA6061 specification, consisting of Mg (0.80–1.20 wt.%), Si (0.40–0.80 wt.%), Cu (0.15–0.40 wt.%), Cr (0.04–0.35 wt.%), Fe (≤0.70 wt.%), Mn (≤0.15 wt.%), Zn (≤0.25 wt.%), Ti (≤0.15 wt.%), with the balance being Al. These compositional limits are specified in ASTM B221 for AA6061 extruded products [15]. Billets were cast by direct-chill (DC) casting and homogenized prior to extrusion at 560 °C for 6 hours to reduce segregation and dissolve coarse intermetallic phases. The homogenized billets had a diameter of 178 mm (7 inches) and a length of 550 mm, yielding a billet mass of approximately 36 kg per charge. The baseline (as-extruded, untreated, T0) mechanical properties of the base material, which serve as the reference condition against which the effects of T6 heat treatment are evaluated in this study, were: Vickers hardness 90–91 HVN, ultimate tensile strength 303–318 MPa, and bending strength 238–421 MPa for the skin and fin regions, respectively.

Extrusion equipment and setup

Extrusion was carried out at a domestic aluminum extrusion manufacturer in Indonesia using a horizontal hydraulic direct extrusion press with a rated capacity of 2.500 metric tons (25 MN) as shown in Figure 1. The press was equipped with a hydraulic power pack consisting of a variable-displacement axial-piston pump driven by a 450-kW electric motor, capable of delivering a maximum system pressure of 350 bar. The main extrusion cylinder had a bore diameter of 250 mm and a stroke of 1,200 mm, providing a maximum ram displacement speed of 12 mm/s. A dummy block of 177.5 mm diameter was employed to ensure full billet expansion against the container wall and to prevent back-flow of material.

The extrusion container (liner) had an internal bore of 178 mm and was maintained at a temperature of 430–450 °C using embedded electrical resistance heaters monitored by four type-K thermocouples distributed along the container length. The container was preheated to the target temperature at least 2 hours prior to the start of the extrusion cycle.

Die design and preparation

A porthole (bridge) die configuration was employed to produce the hollow multi-void

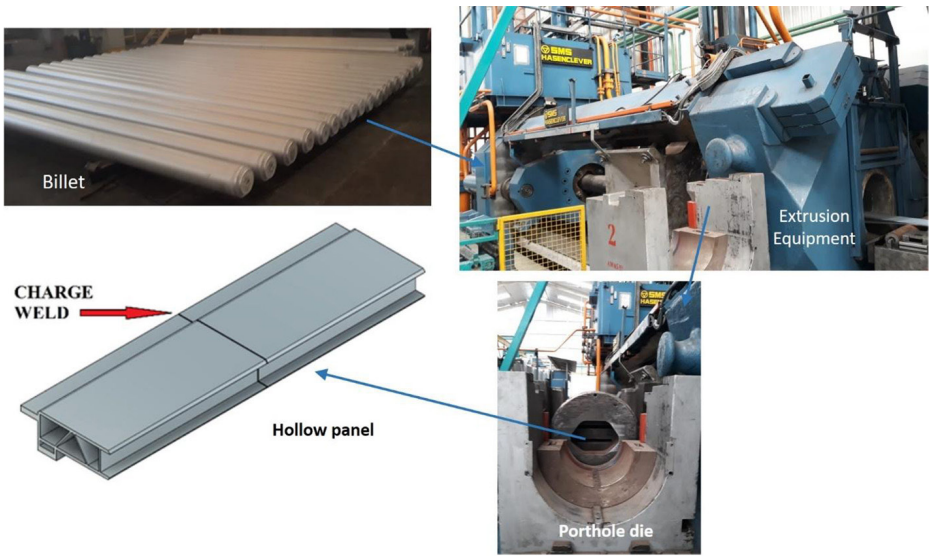

Figure 1. Extrusion equipment

cross-section shown in Figure 2. The die set comprised a mandrel (upper die) with four porthole openings and a die cap (lower die) incorporating the profile bearing channels. The resulting cross-section features a top skin and bottom skin of 2.5 mm nominal thickness, connected by triangulated fins (2 mm thickness) and enclosed at both lateral edges by outer fins (4 mm thickness), yielding an overall profile width of 114.96 mm and a height of 40 mm with an effective cross-sectional area of approximately 610 mm² as seen in Figure 2 (a). The terminology of panel components is illustrated in Figure 2 (b). Bearing land lengths were set at 3–5 mm for the skin sections and 4-6 mm for the internal stiffener walls, determined through die flow simulation to achieve balanced metal flow across all voids simultaneously. This geometry was selected to represent lightweight load-bearing panel configurations representative of those used in transportation flooring and structural decking applications.

The die assembly was fabricated from H13 hot-work tool steel (hardness 48–52 HRC after heat treatment). Prior to each extrusion run, the die set was preheated in a dedicated die oven at 460–480 °C for a minimum of 3 hours to minimize thermal shock and to reduce the extrusion force required at the onset of material flow. Die temperature was verified using a contact pyrometer immediately before installation on the press.

Extrusion process parameters

The billet was heated in a gas-fired induction billet heater to a temperature of 480 ± 10 °C, measured at the billet surface using a contact pyrometer and internally validated with a thermocouple inserted axially into a reference billet. Billet transfer from the heater to the press container was completed within 30 seconds to minimize temperature loss. The principal extrusion parameters adopted in this study are summarized in Table 1.

The extrusion ratio (R) was calculated as the ratio of the container bore cross-sectional area to the total cross-sectional area of the extruded hollow profile (114.96 mm width × 40 mm height, with multiple internal voids as per Figure 2). The ram speed was kept within the range of 3–5 mm/s to control the profile exit temperature and to prevent hot tearing at the weld seams within the porthole die.

Extrusion welding procedure

Because the required panel length of 200 mm in the specimen configuration was used to represent a scaled representation of production panels that would exceed single-billet extrusion capacity in full-scale applications, extrusion welding (*charge welding*) was performed to join two extruded panel segments end-to-end. In a continuous production extrusion press, this condition naturally arises at the charge weld zone, the interface where the trailing end of one billet and the leading end of the subsequent billet are consolidated in the solid state within the porthole die chamber.

In this study, the charge weld was produced under controlled conditions by intentionally introducing a billet-change sequence during the extrusion run. The procedure was as follows:

1. The first billet was extruded until approximately 30 mm of discard remained in the container.

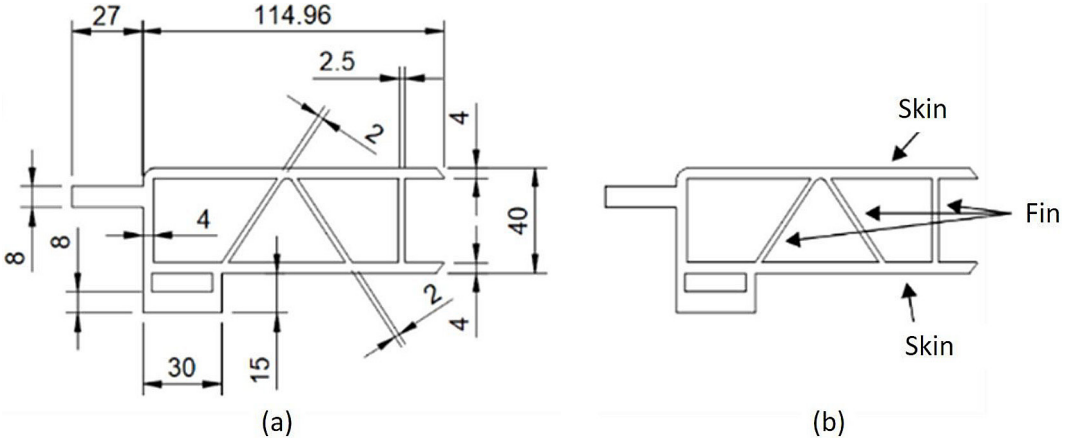

Figure 2. Hollow panel: (a) dimension, (b) terminology of components

Table 1. Summary of extru sion process parameters

Parameter	Value
Press capacity	2.500 metric tons (25 MN)
Container bore diameter	178 mm
Billet diameter	178 mm
Billet length	550 mm
Billet preheat temperature	480 ± 10 °C
Container temperature	430–450 °C
Die preheat temperature	460–480 °C
Ram speed	3–5 mm/s
Extrusion ratio	28:1
Exit profile temperature	500–530 °C (measured by pyrometer at die exit)
Cooling method	Forced air cooling on run-out table

2. The ram was retracted and the residual discard was sheared off using the press shear blade.
3. A second preheated billet (same AA6061 alloy, same dimensions, preheated to 480 ± 10 °C) was loaded and the extrusion cycle resumed immediately.
4. The region of the extruded profile corresponding to the re-start was identified and marked; this region constitutes the charge weld zone (indicated schematically in Figure 3).

Within the porthole die, the metal flowing through the porthole channels from the new billet charge is forced against the retained metal skin from the preceding billet under the prevailing welding pressure, which in porthole dies is generated in the weld chamber located upstream of the bearing land. The welding pressure in this study was estimated at 120–180 MPa based on die geometry and measured ram force, sufficient to achieve intimate metal-to-metal contact and solid-state bonding across the weld interface [16]. No filler material, flux, or shielding gas was employed; the process relies entirely on thermo-mechanical consolidation under pressure. The welding pressure was estimated by converting the peak hydraulic ram force, recorded from the press's integrated load cell during the billet-change cycle, into an equivalent ram pressure using the known ram cross-sectional area, and relating this to the bonding pressure developed within the weld chamber using the die-flow simulation, following the estimation approach outlined by Valberg [5]. The billet-change (shear-and-reload) sequence, comprising ram retraction, shearing of the residual discard, and loading and advance of the new billet, was carried out without any intervening cooling or reheating step, so that the container and die remained at their process temperatures (Table 1) throughout, ensuring that the freshly charged billet material was consolidated against the retained skin under the full process temperature.

Following extrusion, panels containing the charge weld zone at their mid-length were sectioned to a final specimen length of 200 mm using a water-cooled precision abrasive saw. Specimens were grouped into sets corresponding to each T6 heat treatment condition (solution temperature variable), with each set including both weld-zone and base-material regions to enable direct comparative analysis of mechanical and microstructural response.

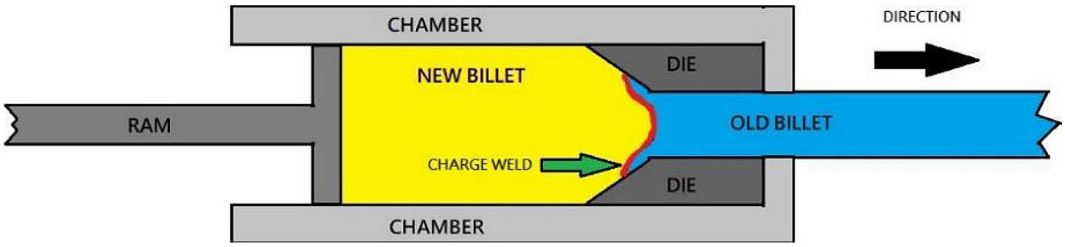

Figure 3. Schematic illustration of extrusion weld (charge weld)

T6 heat treatment

T6 heat treatment was performed using a B-One ceramic muffle furnace. The heat treatment procedure was initially applied only to panels without charge welds in order to determine the optimum solution treatment temperature. Four experimental conditions were established, consisting of an untreated control group (T0) that received no solution treatment, and three solution-treated groups held at 500 °C (T500), 530 °C (T530), and 560 °C (T560), each for a duration of 6 hours. Upon completion of solution treatment, all specimens were immediately quenched in water at ambient temperature. The three solution temperatures examined (500, 530, and 560 °C) were selected to bracket the effective solution treatment window reported for AA6061 and related Al-Mg-Si alloys (approximately 490–560 °C) in prior studies [11,12,17–20], enabling evaluation of the mechanical, microstructural, and corrosion response across sub-optimal, near-optimal, and supra-optimal solution treatment regimes. Artificial aging was subsequently carried out at 200 °C for 6 hours, followed by air cooling to room temperature. After characterization of the panels without charge welds, the optimum solution treatment temperature was identified based on the obtained results. This optimum solution treatment condition was then subsequently applied to the panels containing charge welds for further characterization and evaluation. The complete heat treatment cycle is illustrated schematically in Figure 4.

Characterizations

All characterizations were performed on both skin and stiffener and both panel with and without charge weld. Metallographic specimens were prepared by grinding and polishing the cross-sectional surfaces to a mirror finish. Chemical etching was performed in accordance with ASTM E407, using Keller's reagent composed of 2 mL HF, 3 mL HCl, 5 mL HNO_3, and 190 mL distilled water, with an immersion time of 3 minutes. Macrostructural observation was carried out using an Olympus SZ61 stereomicroscope at magnifications ranging from 0.65× to 4×. Microstructural analysis was performed using a Euromex Holland optical microscope (Euromax, Arnhem, Netherlands) at magnifications of 50× to 500×, enabling assessment of grain morphology and precipitate distribution.

Vickers microhardness measurements were conducted in accordance with ASTM E92, using a diamond pyramid indenter with an included angle of 136° and an applied load of 100 kgf for a dwell time of 10 seconds. Specimens were prepared to a length of 80 mm, and hardness profiles were acquired along 11 measurement points spaced 5 mm apart. Testing was performed using an HWMMT-X7 hardness testing machine.

Uniaxial tensile testing was conducted in accordance with ASTM E8 using a universal testing machine (UTM) SHT-4106 (SANS Testing Machine Co., Shenzhen, China). Specimens were machined to the geometry shown in Figure 5 and loaded monotonically until fracture. Ultimate tensile strength at fracture was recorded.

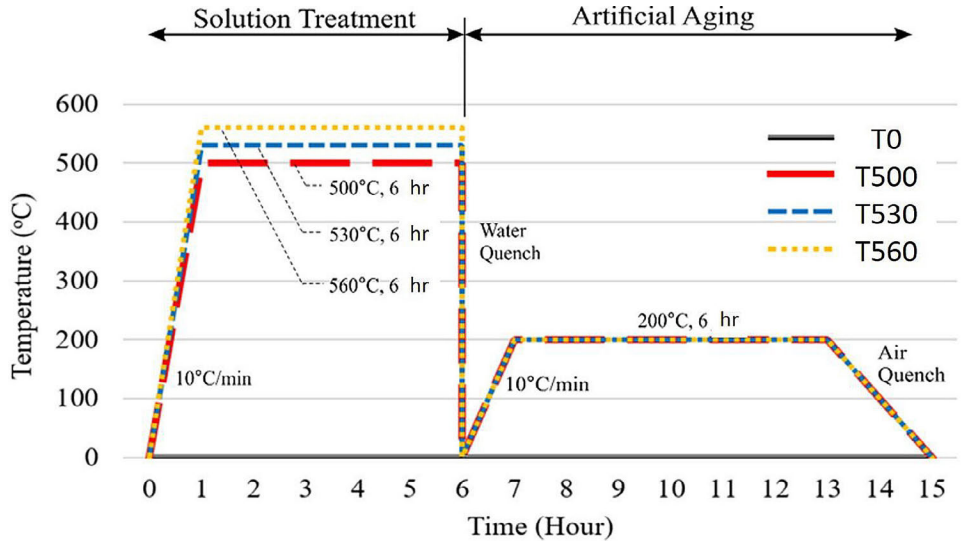

Figure 4. T6 heat treatment process

Three-point bending tests were performed in accordance with ISO 7438 using the same UTM SHT-4106. Specimen geometry is detailed in Figure 6. The bending load was applied at a controlled rate until the prescribed bending angle was achieved or specimen failure occurred.

Electrochemical corrosion tests were conducted in accordance with ASTM G5 using a Corrtest potentiostat immersed in a 3.5 wt% NaCl aqueous solution to simulate a marine environment. A three-electrode cell configuration was employed: a silver-silver chloride (Ag/AgCl) electrode served as the reference electrode, the specimen acted as the working electrode, and a graphite rod was used as the counter electrode. The exposed specimen surface was polished on one side and partially masked with a waterproof sealant to define the active area. Corrosion current density (I_corr) and corrosion potential (E_corr) were extracted from Tafel extrapolation of the resulting polarization curves.

RESULTS AND DISCUSSION

Visual observation following T6 heat treatment

Visual inspection of the AA6061 aluminum extruded hollow panel specimens was conducted following T6 heat treatment to assess the macroscopic surface integrity of each specimen prior to mechanical and microstructural characterization. This qualitative assessment aims to identify physical defects arising directly from the thermal processing conditions. The surface appearance of the specimen subjected to the highest solution treatment temperature of 560 °C (T560) is presented in Figure 7, while the corresponding cross-sectional defect morphology and the schematic blister formation mechanism are shown in Figures 8 and 9, respectively.

As evident in Figure 7, blistering defects were observed on the outer surface of all heat-treated specimens, with the most pronounced manifestations occurring in T560. The surface of T560 exhibited multiple discrete bubble/blistering protrusions distributed across the panel face, with several blister sites accompanied by surface cracking. The co-occurrence of blistering and cracking at the same locations indicates that the gas pressure driving blister formation exceeded the residual strength of the alloy surface layer at the solution treatment temperature of 560 °C.

Cross-sectional examination of T560 specimen, shown in Figure 8, provides further insight into the nature and distribution of these defects. Three distinct defect morphologies were identified: (i) surface blisters without fracture, (ii) blisters accompanied by surface-breaking cracks, and (iii) internal cracks that did not propagate to the outer surface. The defect morphologies observed in this study were classified using the blister/crack terminology established for gas-induced surface discontinuities in aluminum alloys [21–23]. Specifically, a blister is defined as a discrete,

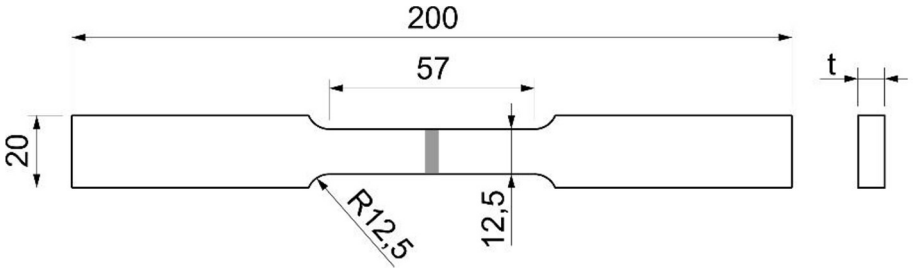

Figure 5. Dimension of tensile testing

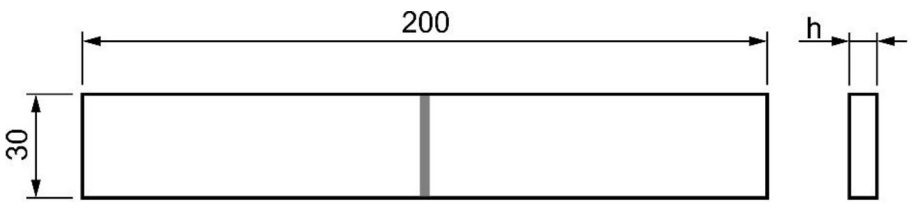

Figure 6. Dimension of bending testing

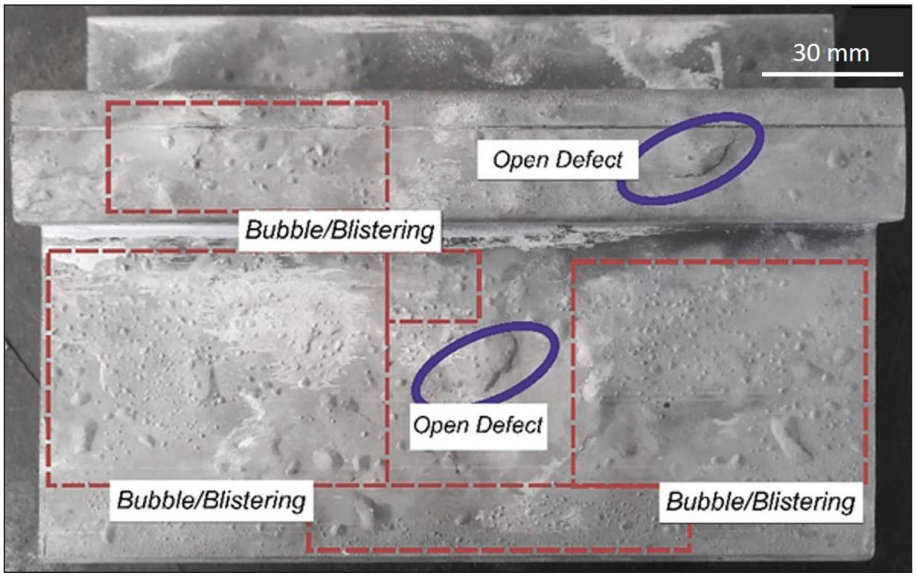

Figure 7. The surface appearance of the specimen subjected to the highest solution treatment temperature of 560 °C (T560)

dome-shaped surface protrusion formed by subsurface gas pressure; a blister-associated (ruptured) crack refers to a blister in which the overlying surface layer has fractured; and an internal (subsurface) crack denotes a void or crack located beneath the surface that does not intersect the free surface. The co-existence of these three morphologies within a single specimen reflects the influence of local geometry, specifically the depth and position of the entrapped gas pocket relative to the surface, and the thickness of the surrounding material, on the resulting defect character. Gas pockets located close to a thin surface layer produced visible blisters and cracks, while gas entrapped deeper within thicker sections generated elongated internal voids, as the surrounding material provided sufficient constraint to suppress outward deformation.

The formation of blistering defects in aluminum alloys during heat treatment is attributed to the thermal expansion of gases primarily hydrogen entrapped beneath the material surface during prior casting or extrusion processing [21–23]. The mechanism is schematically illustrated in Figure 9: when the specimen is exposed to elevated solution treatment temperatures, the entrapped gas expands and exerts an internal pressure (P_{gas}) on the surrounding alloy. When this pressure exceeds the yield force of the softened alloy layer (F_{alloy}), as expressed by the condition $F_{alloy} < P_{gas}$, the surface layer deforms outward, producing a blister. This condition is particularly critical at high solution temperatures, where aluminum alloys are known to experience a substantial reduction in flow stress and tensile strength [21], offering diminished resistance to gas-driven deformation.

The severe cracking observed in T560 specimen is thus a direct consequence of the markedly reduced hot strength of AA6061 at 560 °C, which approaches the upper boundary of the recommended solution treatment range and brings the alloy close to incipient melting conditions. At this temperature, the alloy matrix softens to a degree where the expanding gas not only deforms the surface layer plastically but ruptures it entirely, producing open cracks at the blister perimeter. This finding is consistent with the general understanding that solution treatment temperatures exceeding the safe processing window introduce a risk of incipient melting and surface degradation, particularly in thin-walled geometries such as the skin and fin sections of hollow extrusion profiles [12, 23]. Collectively, these observations establish that the selection of solution treatment temperature must be critically evaluated against the risk of blister-induced surface damage. The geometry of the hollow panel, characterized by thin outer skins and internal fin structures, amplifies this susceptibility relative to bulk specimens. Temperatures at or below 530 °C appeared to limit blistering to isolated surface protrusions without associated cracking, whereas 560 °C induced both surface and subsurface fracture, rendering those specimens structurally compromised.

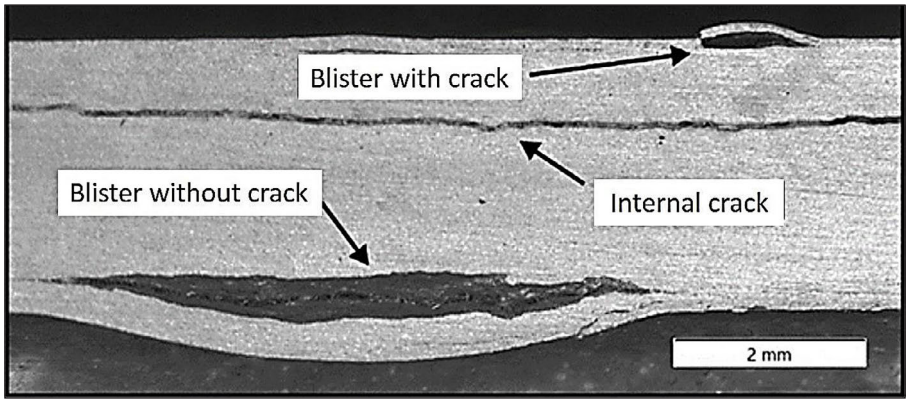

Figure 8. Cross-sectional examination of T560 specimen

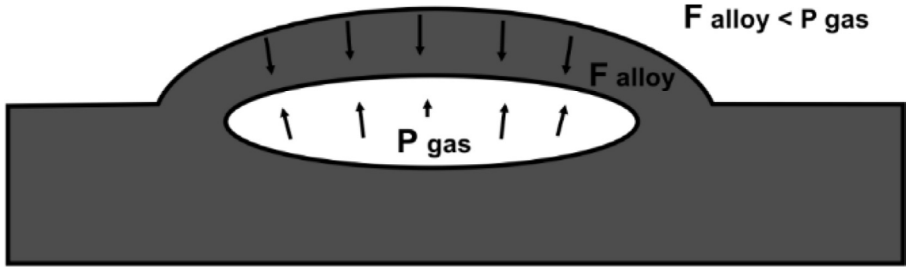

Figure 9. Schematic blister defect formation

Characterization of panels without charge weld

Macrostructure

Macrostructural examination was used to evaluate the extrusion quality of the base material, assess grain morphology changes, and identify surface or subsurface defects arising from T6 heat treatment. The macrostructures of panels without charge welds, observed on both the skin and fin regions, are presented in Figures 10 and 11, respectively. In these figures, T0 designates the as-extruded untreated condition, T500 designates the T6-treated specimen with a solution temperature of 500 °C, T530 corresponds to a solution temperature of 530 °C, and T560 corresponds to 560 °C. In the T0 condition, the skin and fin regions exhibited a fibrous, elongated grain structure oriented along the extrusion direction, consistent with the heavily deformed microstructure characteristic of direct hot extrusion [17,18]. Following T6 treatment at 500 °C and 530 °C, static recrystallization was observed, evidenced by a transition toward more equiaxed grain morphology; this effect was more pronounced at 530 °C, where the higher thermal driving force accelerated grain boundary migration. The T560 condition, in addition to exhibiting the most complete recrystallization, displayed macroscopic evidence of blistering and surface defects consistent with the visual observations, confirming that excessive solution temperature introduces structural degradation that is macroscopically detectable. No signs of incipient melting were observed in T500 or T530 specimens, supporting the selection of these temperatures as within the safe processing window for AA6061 hollow profiles [19, 20].

Microstructure

Optical microstructures of panels without charge welds, acquired from the skin and fin regions, are shown in Figures 12 and 13, respectively. In the T0 condition, both regions displayed elongated, fibrous grains with coarse Mg_2Si and Al-Fe-Si intermetallic particles distributed along grain boundaries, consistent with the as-extruded state [18, 24]. After solution treatment at 500 °C (T500), partial dissolution of coarse Mg_2Si precipitates was evident, with residual undissolved particles remaining at grain boundaries. At 530 °C (T530), more complete precipitate dissolution was achieved, and the distribution of secondary phases became finer and more homogeneous, indicating a higher degree of solid

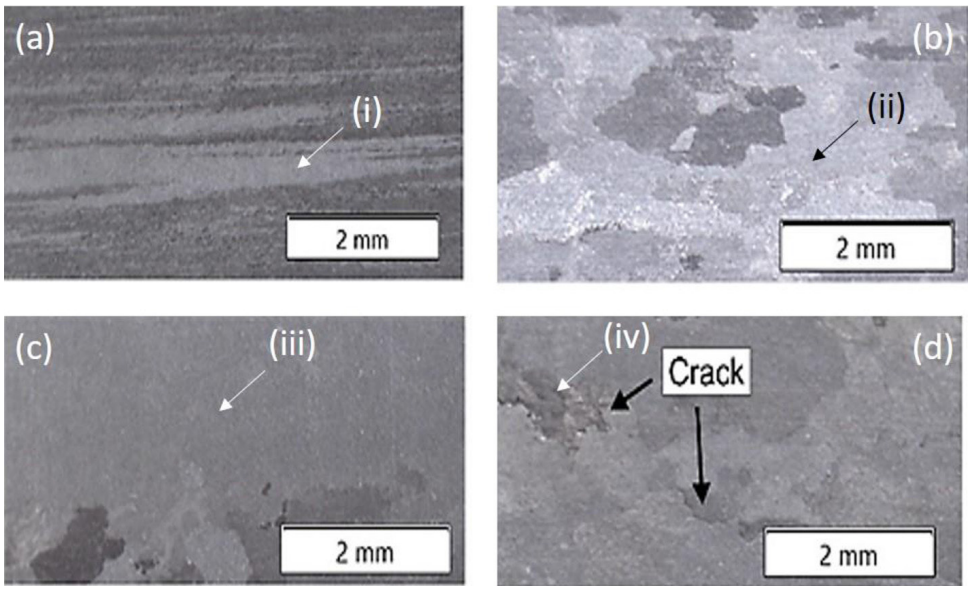

Figure 10. Macrostructure of the skin region: (a) as-extruded without heat treatment (T0), (b) T500, (c) T530, (d) T560 where (i) elongated fibrous grains, (ii) partial recrystallization, (iii) complete recrystallization and (iv) blister-affected region

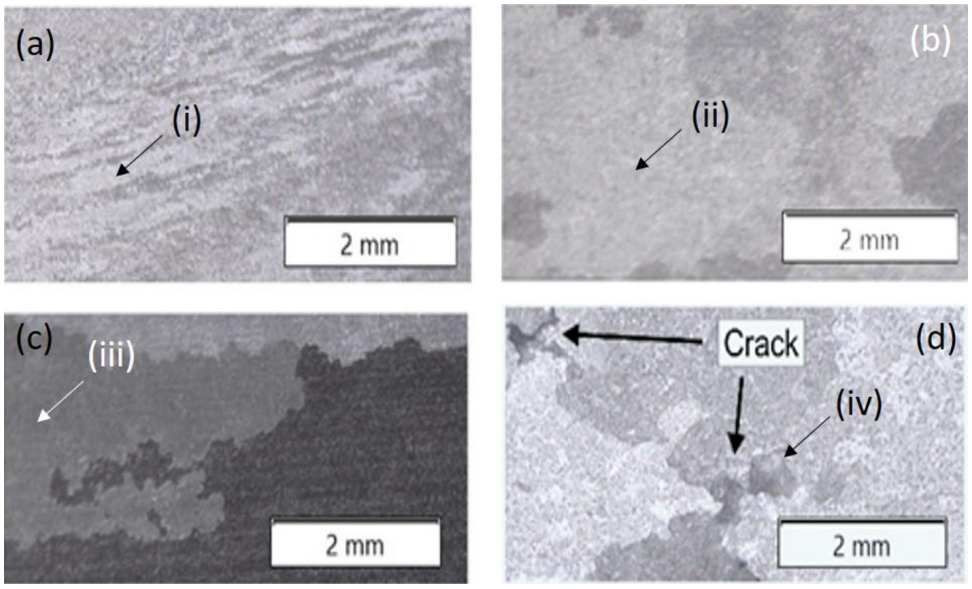

Figure 11. Macrostructure of the fin region: (a) as-extruded without heat treatment (T0), (b) T500, (c) T530, (d) T560, where (i) elongated fibrous grains, (ii) partial recrystallization, (iii) complete recrystallization and (iv) blister-affected region

solution saturation consistent with the literature on optimal solution treatment of AA6061 [17, 20]. The T560 specimens showed evidence of grain boundary liquation and coarsening of intermetallic particles adjacent to blister defect zones, attributed to near-incipient melting conditions at this temperature. These microstructural observations are consistent with the macrostructural and surface integrity findings.

Vickers hardness

The average Vickers hardness measured on skin and fin specimens across all treatment conditions are presented in Figure 14. In the as-extruded T0 condition, both regions exhibited moderate hardness reflecting the work-hardened but un-precipitate-strengthened state. Following T6 treatment at 500 °C, a significant increase in hardness was recorded in both skin

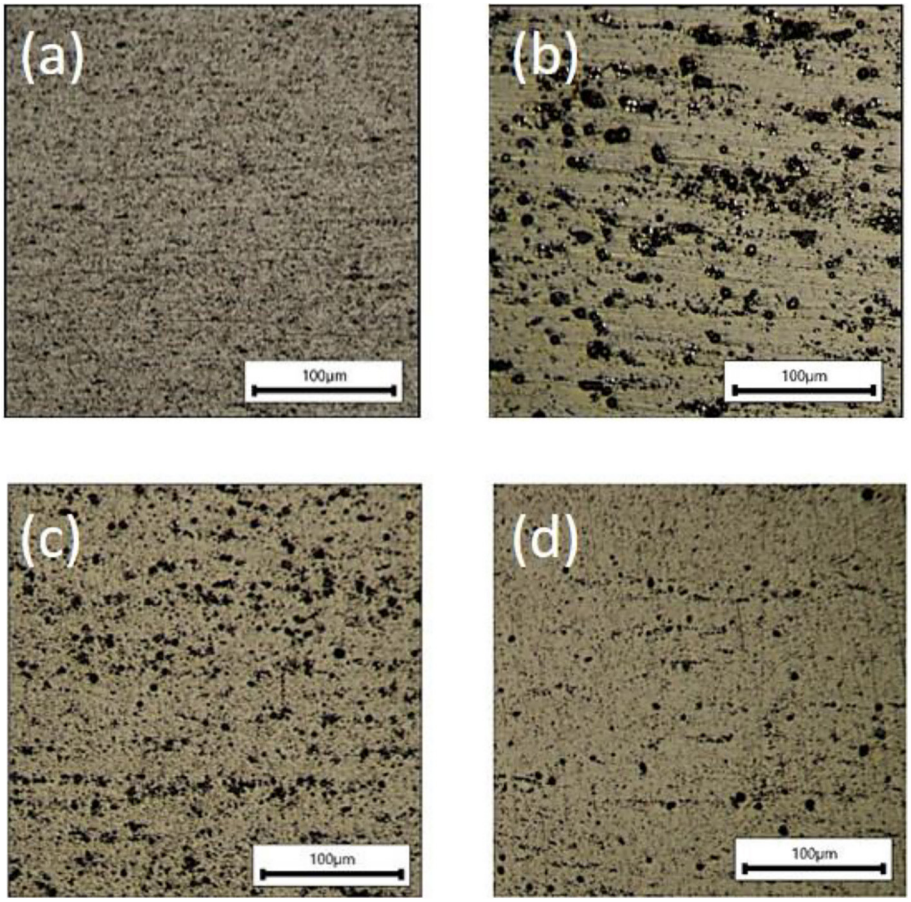

Figure 12. Microstructure of the skin region: (a) as-extruded without heat treatment (T0), (b) T500, (c) T530, (d) T560

and fin regions, attributable to the formation of a dense distribution of fine β″ and β′ precipitates during the subsequent aging step [12, 13]. The T530 condition yielded a further increment in hardness compared to T500, consistent with more complete dissolution of Mg_2Si during the higher-temperature solution stage and a correspondingly higher solute content available for precipitation during aging [17,20]. The T560 specimens, however, showed reduced hardness values relative to T530 despite the highest solution temperature, a finding attributed to grain coarsening, boundary liquation, and the formation of surface defects that compromise load-bearing cross-section integrity [19]. This behavior is consistent with reports by Maisonnette et al. [20] and Lei et al. [17], who noted that hardness peaks at intermediate solution temperatures and degrades above the safe processing window due to microstructural coarsening. The fin region consistently recorded lower hardness than the skin region across all conditions, a difference attributable to the thinner section geometry of the fin and the correspondingly faster cooling rate during quenching, which may alter precipitate size and distribution [25].

Tensile strength

The average tensile properties of panels without charge welds are presented in Figure 15. Fracture morphologies for skin and fin specimens are shown in Figures 16 and 17, respectively. In the T0 condition, both skin and fin specimens exhibited moderate ultimate tensile strength (UTS), consistent with the as-extruded strain-hardened condition without precipitation strengthening. T6 treatment at 500 °C produced a pronounced increase in UTS to T0, as the aging-induced β″ precipitates substantially impede dislocation motion [12, 14]. At 530 °C, a further improvement in tensile strength was observed, attributed to the higher solute concentration taken into solution, which translated into a denser precipitate population during aging. The T560 specimens showed a decline in tensile properties relative to T530, consistent with the microstructural damage

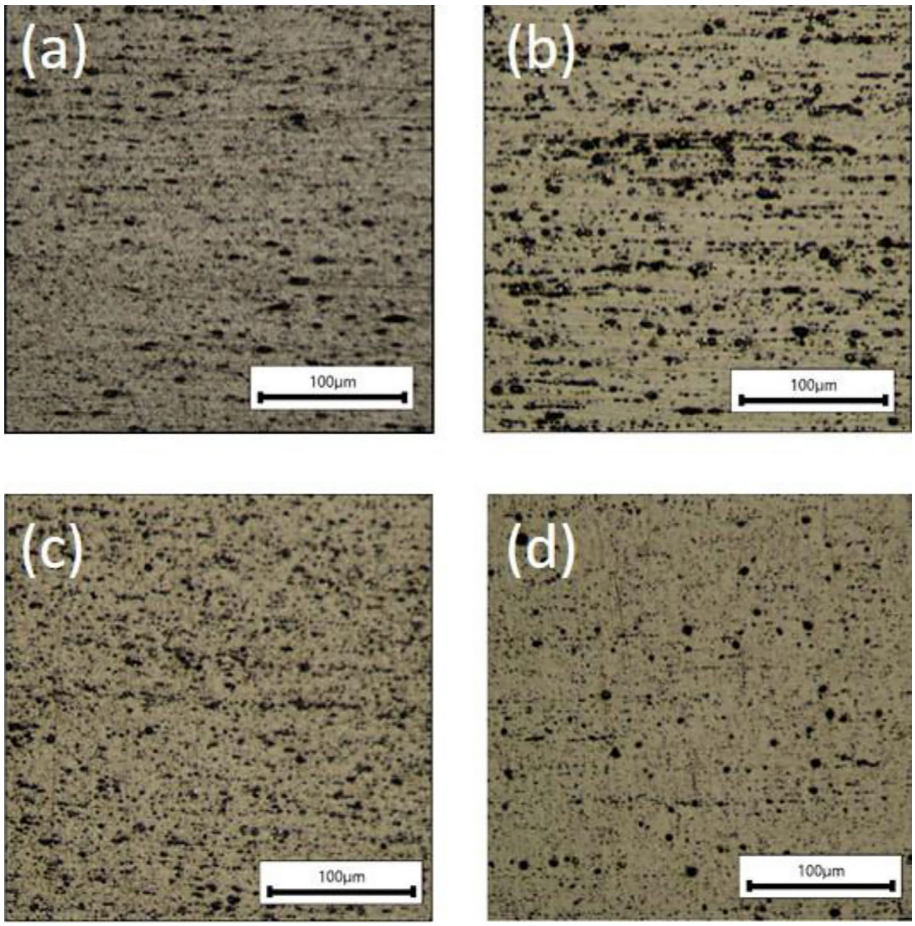

Figure 13. Microstructure of the fin region: (a) as-extruded without heat treatment (T0), (b) T500, (c) T530, (d) T560

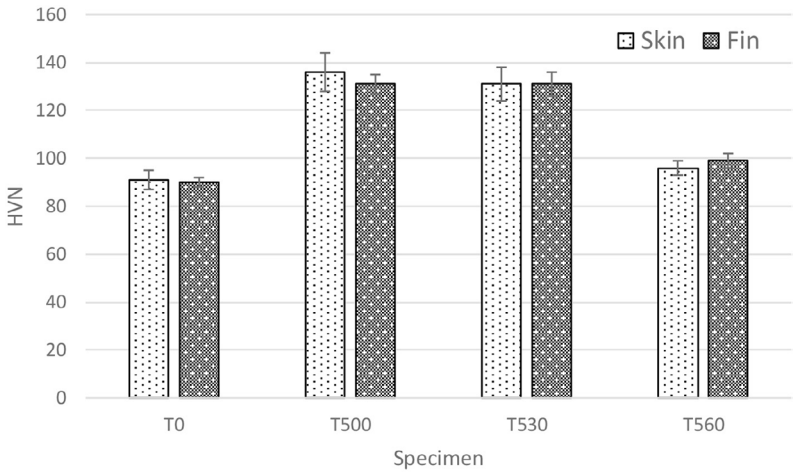

Figure 14. Average Vickers hardness of skin and fin regions for all heat treatment conditions

(grain boundary liquation, blistering, surface cracking). The fracture characteristics observed from the side view of the tensile specimens revealed distinct deformation behaviors among the heat treatment conditions. The T0 specimens exhibited pronounced necking, indicating highly ductile deformation prior to fracture. In the T500 and T530 specimens, necking was still observed but with a noticeably smaller reduction in cross-sectional area, suggesting reduced plastic deformation due to the presence of strengthening precipitates [26]. In contrast, the T560 specimens

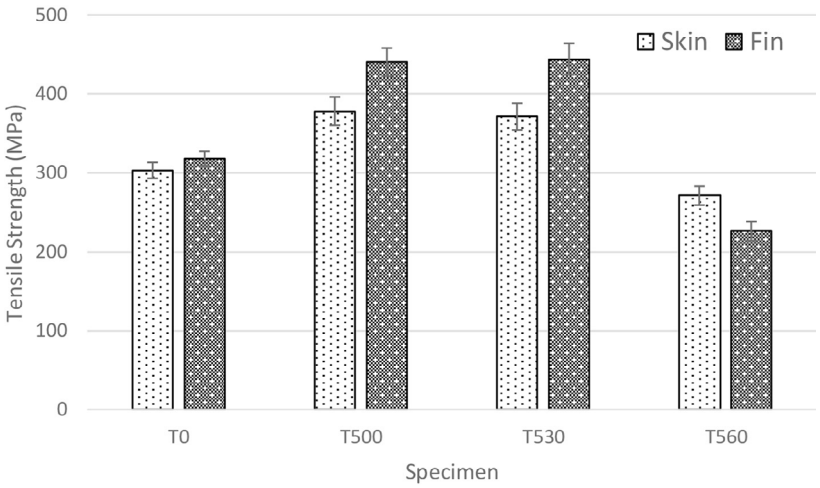

Figure 15. Average tensile strength of skin and fin regions for all heat treatment conditions

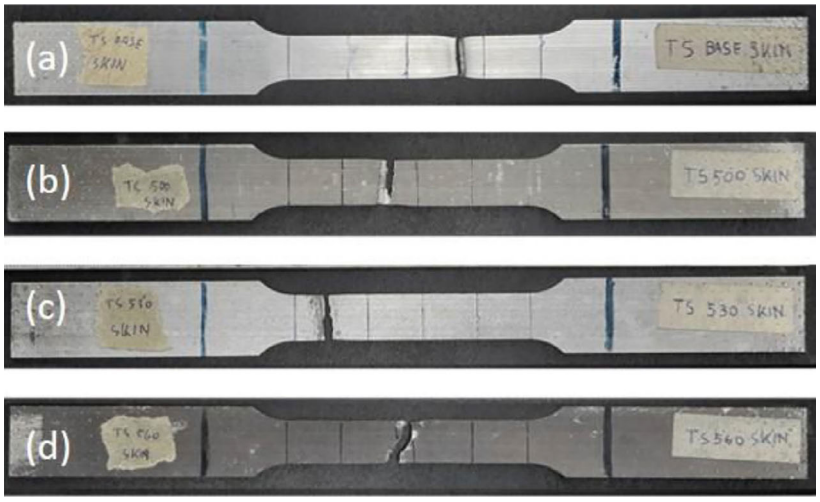

Figure 16. Fracture morphology of skin tensile specimens: (a) as-extruded without heat treatment (T0), (b) T500, (c) T530, (d) T560

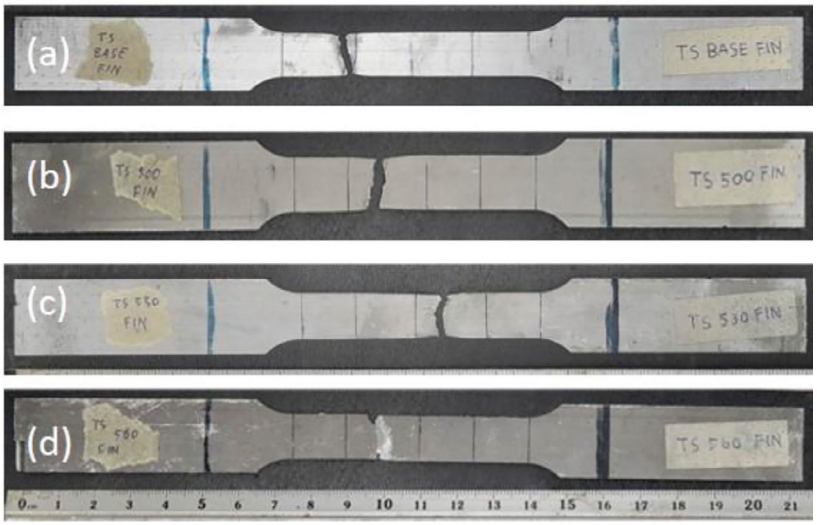

Figure 17. Fracture morphology of fin tensile specimens: (a) as-extruded without heat treatment (T0), (b) T500, (c) T530, (d) T560

showed no visible necking at the fracture location, indicating a more brittle fracture behavior associated with boundary weakening under near-incipient melting conditions. The skin region consistently demonstrated better tensile properties than the fin region under all conditions, which can be attributed to the larger cross-sectional area of the skin and the differences in grain morphology.

Bending strength

The average bending strengths of panels without charge welds are presented in Figure 18. Failure deformation morphologies for skin and fin specimens are shown in Figures 19 and 20, respectively. T6 treatment at 500 °C and 530 °C increased bending strength relative to T0, paralleling the tensile strength trends. The T530 condition achieved the highest bending load capacity among all groups, consistent with the superior precipitate density established at this solution temperature. In contrast, the T560 specimens exhibited a reduction in bending strength and displayed earlier onset of plastic deformation during three-point loading, attributable to surface defects that served as stress concentration sites [27]. Deformation morphologies in T0 specimens were predominantly ductile with large plastic bending radii, while T500 and T530 specimens showed less plastic deformation prior to peak load, reflecting their higher strength and reduced ductility. T560 specimens exhibited premature cracking at blister locations during bending, confirming that surface integrity degradation at excessive solution temperatures directly impairs structural performance under bending loads. These findings are consistent with the literature on the bending behavior of T6-treated aluminum alloys, which reports that solution temperature strongly governs the deformation mode and failure location in thin-walled profiles [27, 28].

Corrosion rate

Tafel polarization diagrams from electrochemical corrosion tests on panels without charge welds are shown in Figure 21(a) for the skin region and Figure 21(b) for the fin region. The calculated corrosion rates for all treatment conditions are presented in Figure 22. In the T0 condition, relatively higher corrosion current densities (Iacc) were recorded, associated with the presence of coarse cathodic Mg_2Si and Al-Fe-Si intermetallics distributed along grain boundaries, which establish galvanic microcells with the aluminum matrix [29, 30]. Following T6 treatment at 500 °C, a reduction in corrosion rate was observed, attributed to partial dissolution of coarse secondary phases and a more homogeneous precipitate distribution that diminishes the electrochemical potential gradient at grain boundaries [29. 31]. The T530 condition exhibited a further improvement in corrosion resistance, with the most negative corrosion potential (Ecc) and lowest Iacc among T6-treated groups, reflecting the most complete dissolution of Mg_2Si at this solution temperature and the subsequent formation of finely dispersed, low-area-fraction precipitates during aging that minimize galvanic coupling [30, 32]. The T560 specimens showed degraded corrosion resistance despite higher solution temperature, attributable to grain boundary liquation, re-precipitation of coarse intermetallics during

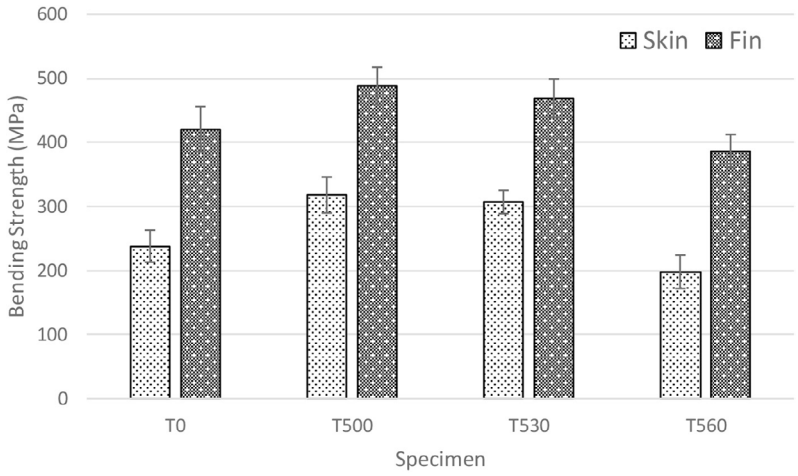

Figure 18. Average bending strength of skin and fin regions for all heat treatment conditions.

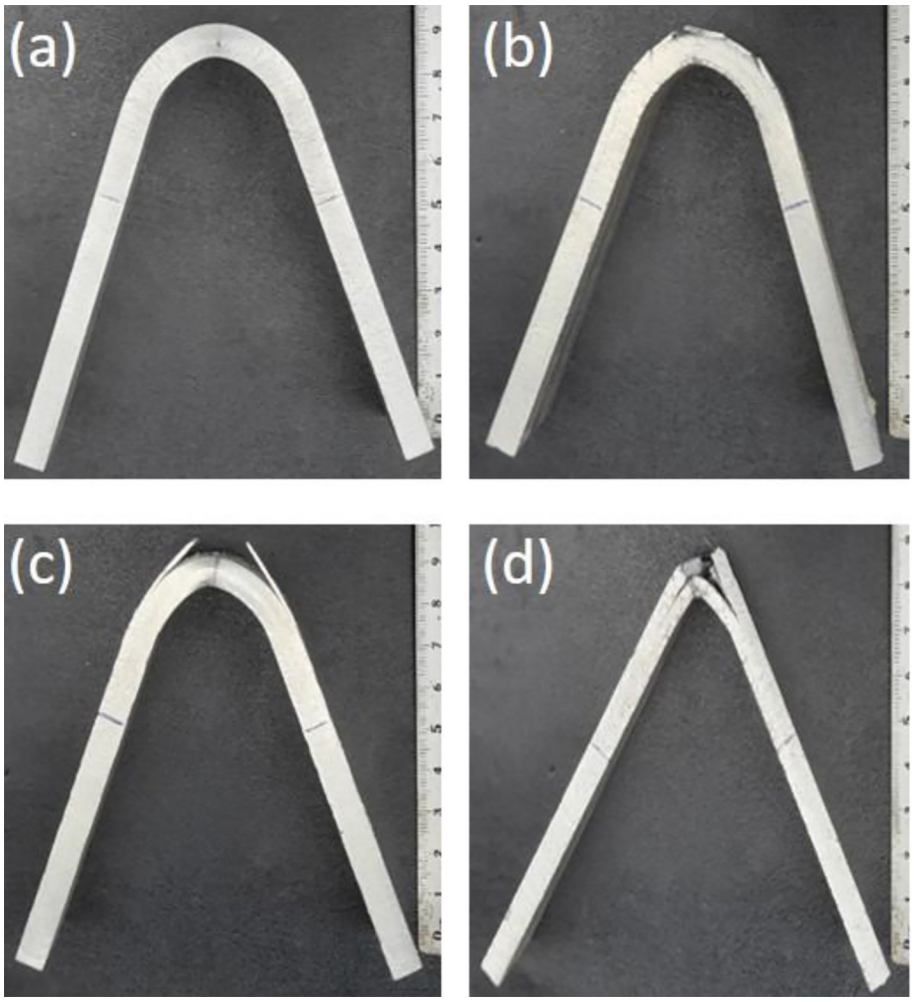

Figure 19. Bending failure deformation of skin specimens: (a) as-extruded without heat treatment (T0), (b) T500, (c) T530, (d) T560

cooling, and surface damage that increased the electrochemically active area [19, 21]. The fin region exhibited slightly higher corrosion rates than the skin region in all conditions, consistent with its thinner section and higher boundary area density. These trends are in agreement with the findings of Zheng et al. [31] and Duan et al. [32] for Al-Mg-Si alloys subjected to varying heat treatment conditions.

Characterization of panels with charge weld

Based on the heat treatment and characterization of panels without charge welds, a solution temperature of 500 °C yielded the best overall combination of mechanical properties, surface integrity, and corrosion resistance. Accordingly, T6 heat treatment with a solution temperature of 500 °C was applied to panels containing charge welds for further characterization. For comparison, the as-extruded untreated condition (T0) was also characterized. In this section, T0 denotes the charge-welded panel without heat treatment, and T500 denotes the charge-welded panel subjected to T6 heat treatment with a solution temperature of 500 °C.

Macrostructure and microstructure

Macrostructural observations of panels containing charge welds are shown in Figure 23. In the T0 condition, the charge weld interface was macroscopically visible as a distinct boundary across the panel cross-section, characterized by a localized disruption of the fibrous extrusion texture. The weld zone displayed a slightly darker contrast under stereomicroscopy, consistent with oxide entrapment and residual grain boundary heterogeneity associated with solid-state bonding under pressure in the porthole die chamber

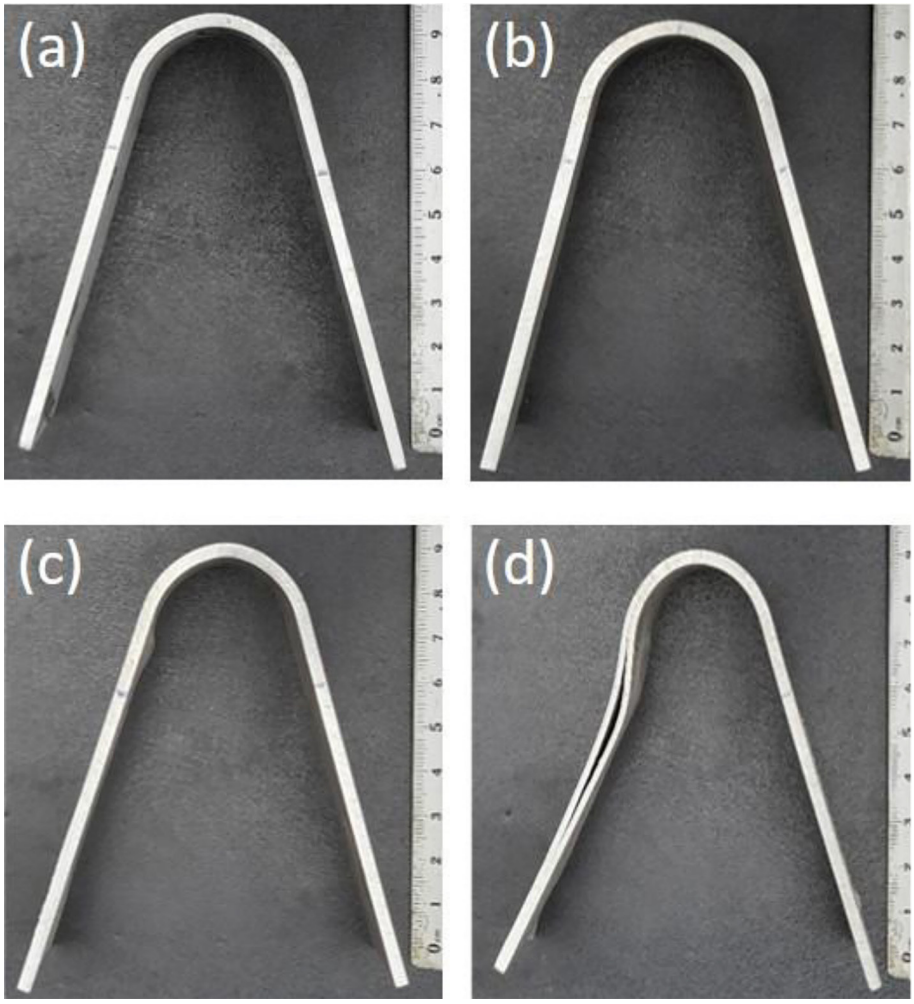

Figure 20. Bending failure deformation of fin specimens: (a) as-extruded without heat treatment (T0), (b) T500, (c) T530, (d) T560

[33, 34]. In the T500 condition, the weld interface became less distinct, indicating that solution heat treatment promoted diffusion across the weld boundary and partial homogenization of the microstructure on either side of the interface. No macroscopic defects such as unbonded regions or cracks were observed in either T0 or T500 specimens, confirming adequate solid-state bonding quality under the extrusion conditions employed [35].

Microstructural examination of the charge weld region was carried out to assess changes in precipitate distribution associated with both the solid-state bonding process and subsequent T6 heat treatment. The microstructures of the charge weld zone for T0 and T500 specimens are shown in Figure 24. In the T0 condition, the weld interface region exhibited a disrupted grain morphology with elongated grains parallel to the extrusion direction transitioning abruptly to more equiaxed grains at the weld line, consistent with the dynamic recrystallization that occurs in the high-deformation weld chamber of porthole dies [33, 34]. Oxide stringers and a slight enrichment of intermetallic particles at the bond interface were also noted, reflecting the limited atomic diffusion across the solid-state bonding interface under extrusion conditions [12, 33]. Following T6 treatment at 500 °C (T500), the precipitate distribution in the weld zone became more homogeneous, with finer and more uniformly dispersed secondary phases compared to the T0 condition. The heat treatment also promoted partial dissolution of coarse interface precipitates, reducing the electrochemical heterogeneity of the weld zone relative to the surrounding base material.

Hardness

The Vickers hardness distribution across the charge weld region is presented in Figure 25. In

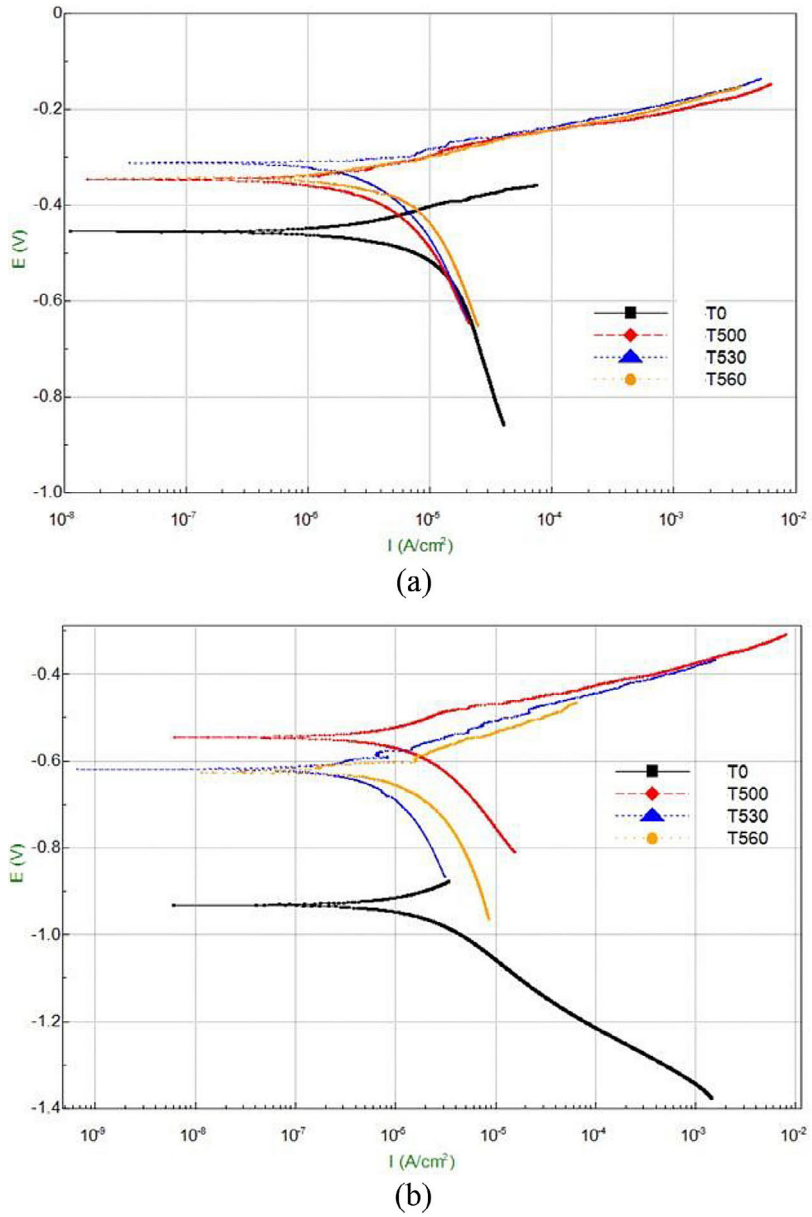

Figure 21. Tafel polarization diagrams of panels without charge welds: (a) skin region and (b) fin region

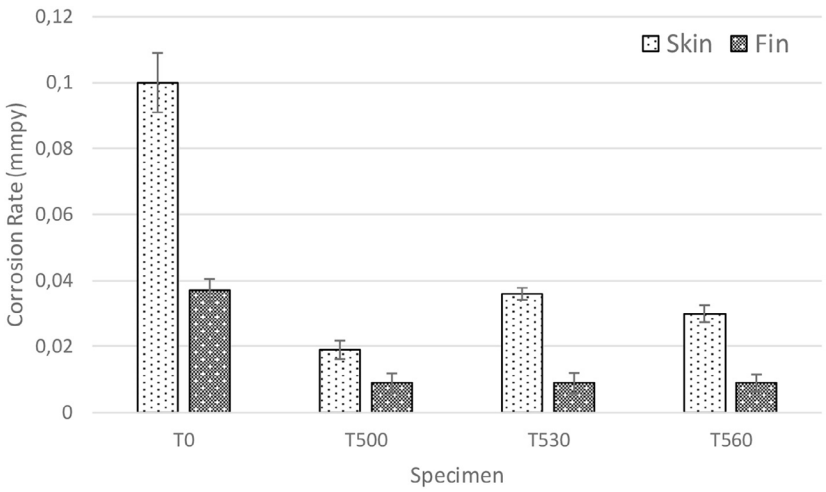

Figure 22. Corrosion rate of panels without charge welds (skin and fin regions)

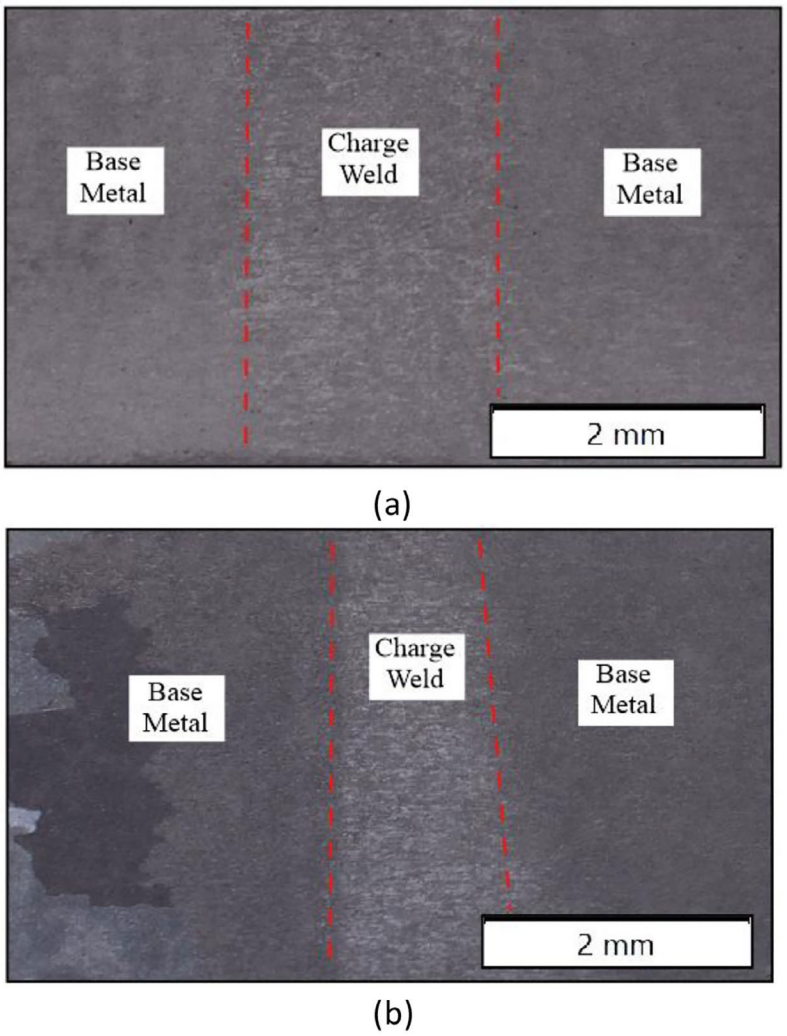

Figure 23. Macrostructure of panels with charge weld: (a) T0 and (b) T500

the T0 condition, a pronounced hardness trough was observed at the weld interface, with hardness in the weld zone measurably lower than those in the adjacent base material regions. This hardness reduction reflects the microstructural heterogeneity at the weld interface, including the disrupted grain morphology, oxide entrapment, and altered precipitate distribution [33, 34]. Following T6 treatment at 500 °C (T500), the hardness profile across the weld zone became more uniform, with weld-zone hardness recovering substantially toward those of the base material. This recovery is attributed to the dissolution and redistribution of Mg_2Si precipitates during solution treatment, followed by re-precipitation of fine β″/β′ phases during aging, which is less sensitive to the prior weld interface microstructure than the as-extruded precipitate distribution. The remaining hardness depression at the weld interface in T500 specimens is consistent with residual oxide stringers and localized grain coarsening that resist full homogenization under the selected solution parameters [12, 13, 33].

Tensile strength

Tensile test results for panels with charge welds are presented in Figure 26. Fracture morphologies for T0 and T500 skin and fin specimens are shown in Figures 27 and 28, respectively. In the T0 condition, tensile specimens containing the charge weld zone exhibited lower UTS compared to the base-material T0 panels, consistent with the weld interface acting as a preferential fracture initiation site due to residual oxide entrapment and grain boundary heterogeneity [33, 34]. Fractures in T0 specimens occurred at or near the weld interface, as confirmed by the fracture locations visible in Figures 27(a) and 28(a). Following T6 treatment at 500 °C, UTS of the charge-welded

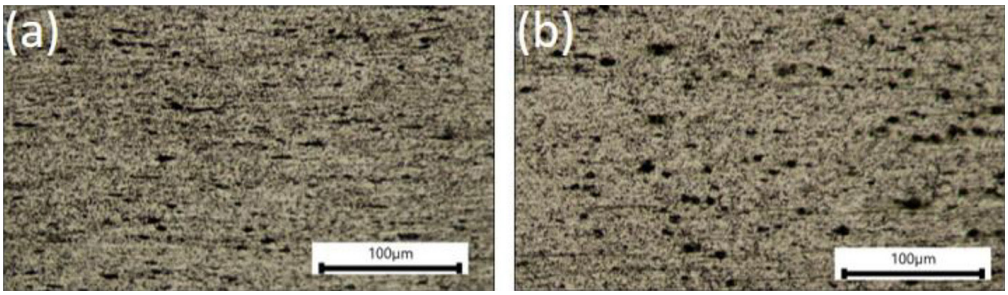

Figure 24. Microstructure of the charge weld zone in panels with charge weld: (a) T0 and (b) T500

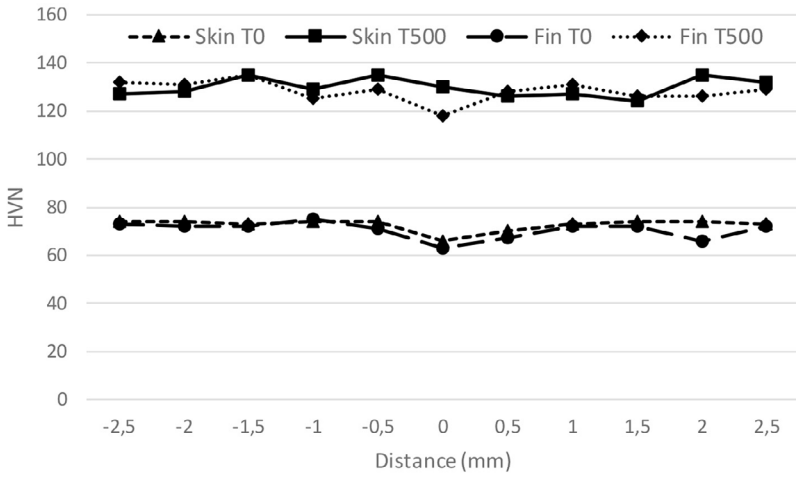

Figure 25. Vickers hardness distribution across the charge weld region

panels increased substantially, approaching but not fully recovering to the T500 base-material values. The remaining strength deficit in T500-welded specimens reflects residual microstructural heterogeneity at the weld interface that persists after solution treatment [12, 33]. T6 treatment at 500 °C significantly improved the load-bearing capacity of the charge-welded panels and, in several specimens, shifted the failure location from the weld interface to the adjacent base material, indicating effective strengthening of the weld zone through precipitation hardening [13, 29].

Bending strength

The bending strength of panels with charge welds is presented in Figure 29. Deformation morphologies from bending tests for T0 and T500 skin and fin specimens are shown in Figures 30 and 31, respectively. In the T0 condition, the charge-welded panels exhibited lower bending peak loads compared to the base-material T0 panels, with fracture or localized deformation initiating at the weld interface, consistent with its lower local hardness and inhomogeneous microstructure [27, 33]. Following T6 treatment at 500 °C, bending strength increased substantially. T500 charge-welded panels showed improved resistance to plastic collapse and a less pronounced deformation asymmetry at the weld interface, indicating that precipitation hardening under the T500 condition partially compensated for the structural weakness introduced by the charge weld. Deformation morphologies in Figure 30 and 31 confirm that T500 specimens sustained larger bending loads before reaching the prescribed deformation limit. The residual bending strength deficit relative to T500 base-material panels is attributed to the persistent microstructural heterogeneity of the weld zone that cannot be fully eliminated by heat treatment alone [12,34].

Corrosion rate

Tafel polarization diagrams from electrochemical corrosion tests on panels containing charge welds are presented in Figure 32(a) for the skin region and Figure 32(b) for the fin region. The calculated corrosion rates for both

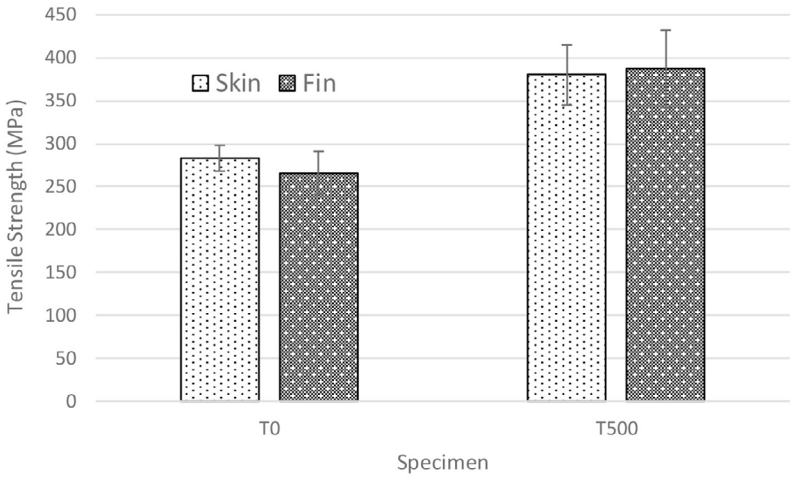

Figure 26. Maximum tensile strength of panels with charge weld

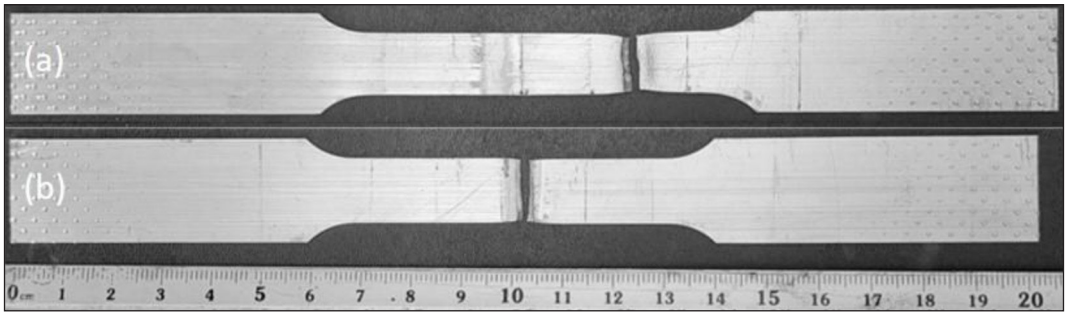

Figure 27. Tensile fracture morphology of T0 specimens: (a) skin, (b) fin

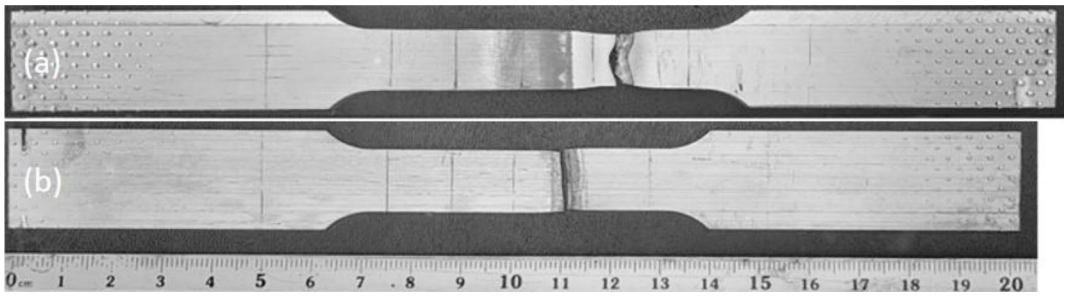

Figure 28. Tensile fracture morphology of T500 specimens: (a) skin, (b) fin

T0 and T500 conditions are summarized in Figure 33. In the T0 condition, the charge weld zone exhibited higher corrosion rates than those recorded in base-material T0 panels, reflecting the electrochemically more active character of the weld interface, where oxide stringers, fine intermetallic particles, and the disrupted grain structure create preferential anodic dissolution sites [30,32,33]. The corrosion potential (Ecc) of the T0 charge-welded specimens was shifted in the anodic direction relative to the base material, while the corrosion current density (Iacc) was correspondingly elevated, consistent with increased galvanic activity at the weld interface [29]. Following T6 heat treatment at 500 °C, the corrosion rate of the charge-welded panels decreased substantially in both skin and fin regions. This improvement is attributed to the homogenization of precipitate distribution across the weld interface, dissolution of coarse cathodic intermetallics, and the formation of a finer, more uniformly distributed β″/β′ precipitate population that reduces the electrochemical potential gradient between the weld zone and the

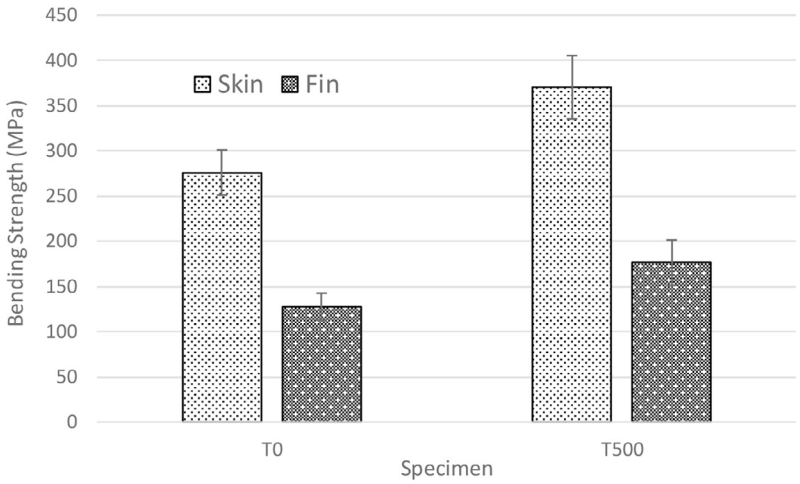

Figure 29. Bending strength of panels with charge weld

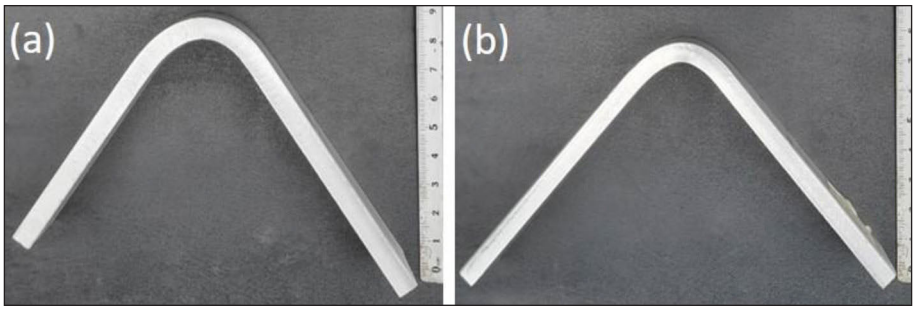

Figure 30. Bending deformation of skin specimens: (a) T0 and (b) T500

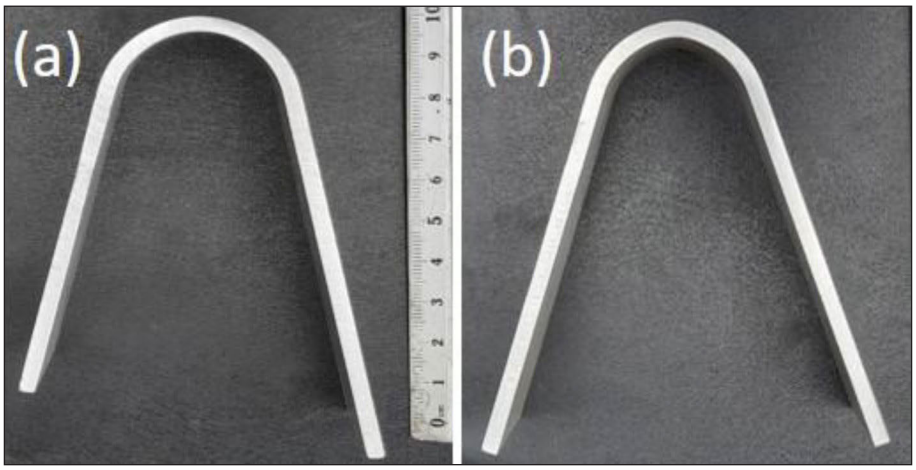

Figure 31. Bending deformation of fin specimens: (a) T0 and (b) T500

surrounding matrix [30, 31, 32]. Although T500 charge-welded specimens still exhibited marginally higher corrosion rates than T500 base-material panels, the difference was considerably reduced compared to the T0 condition, confirming that optimized T6 heat treatment effectively mitigates the enhanced corrosion susceptibility of the charge weld zone.

DISCUSSION

The results collectively establish a coherent process-structure-property framework for T6-treated AA6061 extruded hollow panels, both in base-material form and with charge weld joints. The interdependencies among solution

temperature, microstructural evolution, and the resulting mechanical and corrosion performance are discussed below.

The solution temperature exerts a decisive influence on solute dissolution completeness, which in turn governs the density and distribution of β″ and β′ strengthening precipitates formed during subsequent artificial aging. At 500 °C, Mg and Si are substantially taken into supersaturated solid solution, providing a sufficient solute reservoir for precipitation hardening, while the alloy remains below the incipient melting range and the thin-walled hollow geometry is preserved. At 530 °C, more complete dissolution of residual Mg_2Si is achieved, as reflected in the higher hardness and tensile strength compared to 500 °C, consistent with the well-established relationship between solute concentration and precipitate number density in Al-Mg-Si alloys [12,17,20]. However, the onset of blistering observed in some 530 °C specimens and its severity at 560 °C indicates that entrapped hydrogen in the extrusion stock expands at elevated temperatures to an extent

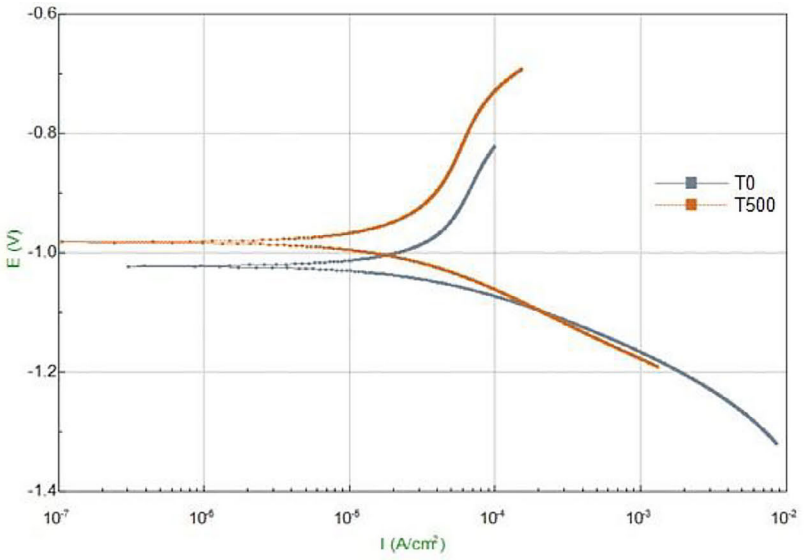

(a)

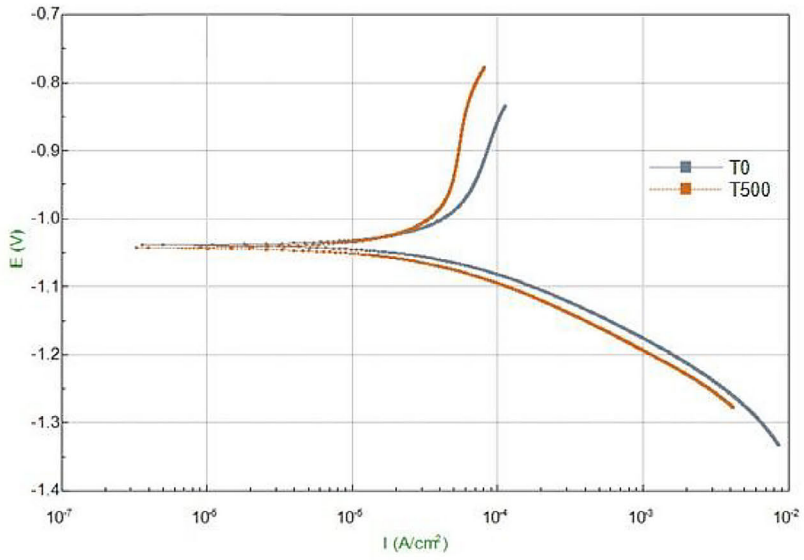

(b)

Figure 32. Tafel polarization diagrams of panels with charge weld: (a) skin region and (b) fin region

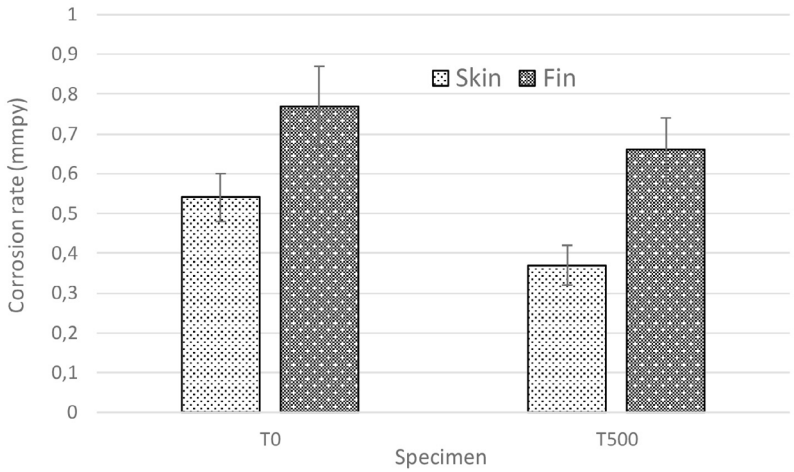

Figure 33. Corrosion rate of panels with charge weld (skin and fin regions)

that the diminished hot flow stress of the alloy cannot resist [21, 22]. This blistering mechanism is especially critical in hollow panel geometries, where thin skins and fins offer less geometric constraint against gas-driven surface deformation than bulk specimens, explaining why defect severity in this study exceeds that reported for solid-section AA6061 at comparable temperatures [23]. The finding that 560 °C produces both the most complete microstructural homogenization and the greatest surface damage confirms that, for hollow extruded profiles of this geometry, the effective solution treatment window is bounded above by the blistering threshold rather than by the thermodynamic solvus.

The selection of 500 °C as the optimum solution temperature for this hollow panel geometry reflects a balance between solute dissolution efficiency and thermal safety. While T530 produced marginally superior hardness and tensile properties in the absence of blistering in most specimens, the risk of surface damage in thin-walled sections at this temperature introduces unacceptable variability for structural applications. The 500 °C condition consistently delivered improved mechanical properties over the as-extruded state without compromising surface integrity, in agreement with previous findings for AA6061 and related Al-Mg-Si alloys in which solution temperatures between 490 and 520 °C are recommended to balance dissolution efficiency and thermal safety for thin-section profiles [17–20].

The charge weld zone is the dominant source of structural heterogeneity in long-length extruded hollow panels and represents the primary engineering challenge addressed by this study. In the as-extruded (T0) condition, the weld zone exhibits systematically lower hardness, tensile strength, and bending resistance than the surrounding base material, and higher corrosion susceptibility, attributable to the combined effects of residual oxide entrapment, grain boundary disruption, and altered precipitate distribution at the solid-state bond interface [33, 34]. These properties place the weld zone as the weakest link in the structural assembly, rendering knowledge of its response to T6 heat treatment critical for the safe design of charge-welded panel structures.

The application of T6 treatment at 500 °C to charge-welded panels substantially mitigated the property deficit of the weld zone. The recovery of hardness, tensile strength, and bending strength toward base-material T500 values is mechanistically consistent with the dissolution and re-precipitation of Mg_2Si-type phases during T6 cycling: the solution stage dissolves the existing coarse precipitate distribution, regardless of its prior morphology at the weld interface, and the aging stage re-precipitates a fine, uniform β″/β′ population that is relatively insensitive to the prior weld boundary microstructure [12, 13, 29]. The residual property deficit between T500 weld-zone and T500 base-material specimens can be attributed to persistent oxide stringers and localized grain coarsening at the weld interface that are not dissolved during the solution stage and continue to act as preferential fracture initiation and anodic dissolution sites. This finding has an important practical implication: T6 heat treatment can serve as an effective

post-processing step to partially homogenize the mechanical and corrosion properties of charge-welded hollow extrusion panels, reducing but not entirely eliminating the property contrast between the weld zone and the base material.

The corrosion behavior of both base-material and charge-welded panels is governed by the distribution and electrochemical activity of secondary phases relative to the aluminum matrix. In the as-extruded condition, coarse Mg_2Si and Al-Fe-Si intermetallics at grain boundaries act as cathodic sites that accelerate anodic dissolution of the surrounding matrix, producing pitting and intergranular corrosion in 3.5 wt.% NaCl solution [30, 32]. T6 treatment at 500 °C reduces the cathodic area fraction of coarse intermetallics through partial dissolution during the solution stage, and the fine β″/β′ precipitates formed during aging are less electrochemically active than coarse Mg_2Si, resulting in a more uniform corrosion front and a reduced net corrosion rate [30, 31]. The improvement in corrosion resistance of the weld zone under T500 relative to T0 follows the same mechanistic pathway, with the additional benefit that the partial homogenization of the interface microstructure reduces the preferential anodic activity at the weld line. These trends align with the broader literature on the corrosion behavior of heat-treated Al-Mg-Si alloys, in which T6 tempers consistently outperform as-extruded or over-aged conditions in 3.5 wt.% NaCl environments [31, 32].

Taken together, these results demonstrate that the combination of a controlled charge weld extrusion process and an optimized T6 treatment at 500 °C enables the production of lightweight AA6061 hollow extrusion panels of extended length with mechanical and corrosion properties that are structurally viable for transportation flooring, structural decking, and similar load-bearing applications. The key engineering insight is that neither the charge weld nor the T6 heat treatment alone is sufficient: the weld requires T6 treatment to recover its properties, and T6 treatment requires the correct solution temperature to avoid the compounding problem of surface damage in thin-walled profiles. The quantitative process, structure-property relationships established here provide a mechanistic basis for rational heat treatment schedule design and constitute a reference dataset for structural designers specifying AA6061 hollow extrusion panels with charge weld joints.

CONCLUSIONS

This study systematically investigated the influence of solid solution temperature in T6 heat treatment on the microstructure, mechanical properties, and corrosion behavior of AA6061 extruded hollow panels, with and without charge weld joints. Based on the experimental findings, the following conclusions are drawn:

1. Solution treatment at 560 °C induced severe blistering and surface cracking on the hollow panel surface, attributed to the expansion of entrapped hydrogen gases under the substantially reduced hot flow stress of AA6061 at near-incipient melting conditions. This defect mode was not observed at 500 °C and was limited to isolated protrusions without associated cracking at 530 °C, confirming that thin-walled hollow extrusion profiles of this geometry have a narrower safe solution treatment window than bulk specimens.
2. Among the solution temperatures investigated, 500 °C was identified as optimal for panels without charge welds, delivering the best balance of surface integrity, Vickers hardness, tensile strength, bending strength, and corrosion resistance. Relative to the as-extruded condition, T6 treatment at 500 °C increased Vickers hardness from 90–91 HVN to131–136 HVN, ultimate tensile strength from 303–318 MPa to 378–440 MPa, bending strength from 238-421 MPa to 318–489 MPa, and reduced the corrosion rate from 0.037–0.10 mm/y to 0.009–0.019 mm/y. Microstructural analysis confirmed that 500 °C achieved substantial Mg_2Si dissolution and promoted formation of a fine, homogeneous β″/β′ precipitate distribution during aging, without inducing grain boundary liquation or surface damage.
3. The skin region of the hollow panel consistently outperformed the fin region in hardness, tensile strength, and bending strength across all treatment conditions, attributable to the larger cross-sectional area of the skin, differences in grain morphology, and the higher cooling rate experienced by the thinner fin section during quenching.
4. In the as-extruded condition (T0), charge weld joints exhibited measurably lower hardness, tensile strength, bending strength, and corrosion resistance compared to the surrounding

base material, with fracture consistently initiating at the weld interface, reflecting its microstructural heterogeneity, oxide entrapment, and locally altered precipitate distribution.

5. T6 heat treatment at 500 °C substantially recovered the mechanical properties and corrosion resistance of charge-welded panels, with the weld zone hardness, tensile strength, and bending strength approaching those of the T500 base material. Tensile strength of the weld region increased from 266–283 MPa to 380–387 MPa, bending strength from 127.5–276 MPa to 176–370 MPa, and corrosion rate decreased from 0.54–0.77 mm/y to 0.37–0.66 mm/y. This recovery is attributed to the dissolution and uniform re-precipitation of β″/β′ strengthening phases across the weld interface during the T6 cycle. A residual property deficit relative to the base material persists, attributed to the irreducible microstructural heterogeneity (persistent oxide stringers, residual grain boundary disruption) at the charge weld interface.
6. T6 treatment at 500 °C improved the corrosion resistance of both base-material and charge-welded panels in 3.5 wt.% NaCl solution, with lower corrosion current densities and more negative corrosion potentials relative to the T0 condition, attributable to the dissolution of coarse cathodic intermetallics and the formation of a less electrochemically active precipitate population during aging. The corrosion rate of the charge weld zone was substantially reduced under T500, approaching base-material T500 values, confirming that optimized T6 treatment mitigates the enhanced corrosion susceptibility of the weld interface. Specifically, the corrosion rate of the charge weld zone decreased from 0.54–0.77 mm/y at T0 to 0.37–0.66 mm/y at T500, a reduction of approximately 24–31%.

Acknowledgements

The authors gratefully acknowledge the support of Universitas Sebelas Maret, Lembaga Pengelola Dana Pendidikan (LPDP), and the National Research and Innovation Agency of Indonesia (BRIN) for providing research facilities and financial support through the RIIM 2022 grant (Contract No. 1562.1/UN27.22/HK.07.00/2022). The authors also thank the students of the METALS Research Group for their assistance during the experimental work. In addition, the authors acknowledge the use of language-support tools, including Claude Ai, for English proofreading and paraphrasing during the manuscript preparation.

REFERENCES

1. Singh S. P., George D.X.T., Xavier A. A. J., and Raja G. A., Effect of heat treatment on the hardness behaviour of the aluminium 6061 alloy. Materials Today: Proceedings, Mar. 2023, https://doi.org/10.1016/j.matpr.2023.02.345
2. Peng J., Bahl S., Shyam A., Haynes J. A., and Shin D., Solute-vacancy clustering in aluminum, Acta Mater, 2020; 196: 747–758, https://doi.org/10.1016/j.actamat.2020.06.062
3. Yürük A., Çevik B., and Kahraman N., Analysis of mechanical and microstructural properties of gas metal arc welded dissimilar aluminum alloys (AA5754/AA6013), Mater Chem Phys, 2021; 273: 125117, https://doi.org/10.1016/j.matchemphys.2021.125117
4. You X., Xing Z., Jiang S., Zhu Y., Lin Y., Qiu H., Nie R., Yang J., Hui D., Chen W., and Chen Y., A review of research on aluminum alloy materials in structural engineering. Developments in the Built Environment, 2024; 17: 100319, https://doi.org/10.1016/j.dibe.2023.100319
5. Valberg H., Extrusion welding in aluminium extrusion, *International Journal of Materials and Product Technology*, 2002; 17(7): 497–556, https://dx.doi.org/10.1504/IJMPT.2002.001317
6. Bingöl S. and Bozacı A., Experimental and numerical study on the strength of aluminum extrusion welding, *Materials*, 2015; 8(7): 4389–4399, https://doi.org/10.3390/ma8074389
7. Zhang X., Feng D., Shi X., Liu S., Oxide distribution and microstructure in welding zones from porthole die extrusion, *Transactions of Nonferrous Metals Society of China*, 2013; 23(3): 765–772, https://doi.org/10.1016/S1003-6326(13)62527-3
8. Yao S.J., Tang Q.H., Yang J., Wang C.Y., Sun H.F., Rong R.L., Sun H.R., and Chu G.N., Microstructural characterization and mechanical properties of 6061 aluminum alloy processed with short-time solid solution and aging treatment. Journal of Alloys and Compounds, 2023; 960: 170704, https://doi.org/10.1016/j.jallcom.2023.170704
9. Liu Y., Fang D., Zhu B., Wang Y., Li S. and Zhang Y., Modeling of isothermal dissolution of precipitates in a 6061 aluminum alloy sheet during solution heat treatment, *Metals*, 2021; 11(8), art. no. 1234, https://doi.org/10.3390/met11081234
10. Edwards G.A., Stiller K., Dunlop G.L., Couper

M.J., The precipitation sequence in Al–Mg–Si alloys, Acta Materialia, 1998; 46(11): 3893–3904, https://doi.org/10.1016/S1359-6454(98)00059-7

11. Sun H., Xing S., Zhao B., Jiang X., Xu X., Study on the influence of solution temperature on the synergistic effect of precipitation strengthening and fine grain strengthening of AA6061, *Materials Today Communications*, Dec. 2022; 33: 104312, https://doi.org/10.1016/j.mtcomm.2022.104312
12. Fröck H., Milkereit B., Wiechmann P., Springer A., Sander M., Kessler O., and Reich M., Influence of solution-annealing parameters on the continuous cooling precipitation of aluminum alloy 6082, *Metals,* 2018; 8(4): 265, https://doi.org/10.3390/met8040265
13. Wang Y., Zhao G., Sun L., Wang X., Lv Z., and Sun Y., Effects of billet heating temperature and extrusion speed on the microstructures and mechanical properties of the longitudinal welds in aluminum alloy profiles with complex cross-section, Vacuum, Jan. 2023; 207, https://doi.org/10.1016/j.vacuum.2022.111578
14. Bölükbaşı D. Ç., Aslanlar S., and Konar M., Investigation of parameters affecting longitudinal seam quality of aluminum extruded profiles, J Radiat Res Appl Sci, Dec. 2023; 16(4): 100700, https://doi.org/10.1016/j.jrras.2023.100700
15. ASTM B221-14, Standard Specification for Aluminum and Aluminum-Alloy Extruded Bars, Rods, Wire, Profiles, and Tubes, ASTM International, West Conshohocken, PA, 2014.
16. Yu J., Zhao G., Chen L., W., Analysis of longitudinal weld seam defects and investigation of solid-state bonding criteria in porthole die extrusion process of aluminum alloy profiles, Journal of Materials Processing Technology, 2016; 237: 342–350, https://doi.org/10.1016/j.jmatprotec.2016.05.024
17. Lei G., Wang B., Lu J., Wang C., Li Y., and Luo F., Effects of solid solution temperature on the microstructure and properties of 6013 aluminum alloy. Materials Chemistry and Physics, Mar. 2022; 280: 125829, https://doi.org/10.1016/j.matchemphys.2022.125829
18. Aydi L., Khlif M., Bradai C., Spigarelli S., Cabibbo M., and Mehtedi M.E., Mechanical properties and microstructure of primary and secondary AA6063 aluminum alloy after extrusion and T5 heat treatment. Materials Today: Proceedings, 2015; 2(10): 4890–4897, https://doi.org/10.1016/j.matpr.2015.10.044
19. Berndt N., Frint P., Böhme M., and Wagner M.F.-X., Microstructure and mechanical properties of an AA6060 aluminum alloy after cold and warm extrusion. Materials Science and Engineering: A, Nov. 2017; 707: 717–724, https://doi.org/10.1016/j.msea.2017.09.040
20. Maisonnette D., Suery M., Nelias D., Chaudet P., and Epicier T., Effects of heat treatments on the microstructure and mechanical properties of a 6061 aluminium alloy. Materials Science and Engineering: A, Mar. 2011; 528(6): 2718–2724, https://doi.org/10.1016/j.msea.2010.12.011
21. Hu X.G., Zhu Q., Midson S.P., Atkinson H.V., Dong H.B., Zhang F., and Kang Y.L., Blistering in semi-solid die casting of aluminium alloys and its avoidance, Acta Materialia, Feb. 2017; 124: 446–455, https://doi.org/10.1016/j.actamat.2016.11.032
22. Keitaro H., andIshii A. Effect of purity on the internal morphology of blisters on aluminum surfaces." Results in Materials, Mar. 2024; 21: 100522, https://doi.org/10.1016/j.rinma.2023.100522
23. Horikawa K., Taniyama M., and Kobayashi H., Morphological observation of blisters generated in a high purity aluminum plate. J. Jpn. Inst. Light Metals, 2020; 70: 432–434, https://doi.org/10.2464/jilm.70.432
24. Asghar G., Peng L., Fu P., Yuan L., and Liu Y., Role of Mg_2Si precipitates size in determining the ductility of A357 cast alloy. Materials & Design, Jan. 2020; 186: 108280, https://doi.org/10.1016/j.matdes.2019.108280
25. Tang H-P., Wang Q-D., Lei C., Ye B., Wang K., Jiang H-Y., Ding W-J., Zhang X-F., Lin Z., and Zhang J-B., Effect of cooling rate on microstructure and mechanical properties of an al-5.0Mg-3.0Zn-1.0Cu cast alloy. Journal of Alloys and Compounds, Sept. 2019; 801: 596–608, https://doi.org/10.1016/j.jallcom.2019.06.002
26. Muhammad W., Brahme A. P., Sabat R. K., Mishra R. K., and Inal K., A criterion for ductile failure in age-hardenable aluminum alloys. Materials Science and Engineering: A, 2019; 759: 613–623, https://doi.org/10.1016/j.msea.2019.05.055
27. Liu Z., Li L., Yi J., Li S., Wang Z., and Wang G., Influence of heat treatment conditions on bending characteristics of 6063 aluminum alloy sheets. Transactions of Nonferrous Metals Society of China, July 2017; 27(7): 1498–1506, https://doi.org/10.1016/S1003-6326(17)60170-5
28. Aune S., Morin D., Langseth M., and Clausen A. H., Experimental and numerical study on the tensile ductility of an aluminium alloy with heat-affected zones, Eur. J. Mech./A Solids, 2024; 105: 105239, https://doi.org/10.1016/j.euromechsol.2024.105239
29. Kim J., Shin S., and Lee S., Correlation between microstructural evolution and corrosion resistance of hypoeutectic Al-Si-Mg alloy: Influence of corrosion product layer, Mater. Charact., April, 2022; 193, https://doi.org/10.1016/j.matchar.2022.112276
30. Zeng F. L., Wei Z. L., Li J. F., Li C. X., Tan X., Zhang Z., and Zheng Z. Q., Corrosion mechanism

associated with Mg_2Si and Si particles in Al-Mg-Si alloys, Trans. Nonferrous Met. Soc. China, 2011; 21(12): 2559–2567, https://doi.org/10.1016/S1003-6326(11)61092-3

31. Zheng C., Chen X., Li C., Shen X., andCheng K., The effect of heat treatment on corrosion resistance of 6061 aluminum alloy. International Journal of Electrochemical Science, Aug. 2016; 11(8), 7254–7261, https://doi.org/10.20964/2016.08.35
32. Duan C., Tang J., Ma W., Ye L., Jiang H., Deng Y., and Zhang X., Intergranular corrosion behavior of extruded 6005A alloy profile with different microstructures, J. Mater. Sci., 2020; 55: 10833–10848, https://doi.org/10.1007/s10853-020-04692-6.
33. Den Bakker A. J., Katgerman L., and Van Der Zwaag S., Analysis of the structure and resulting mechanical properties of aluminium extrusions containing a charge weld interface, J Mater Process Technol, Mar. 2016; 229: 9–21, https://doi.org/10.1016/j.jmatprotec.2015.09.013
34. Yu J. and Zhao G., Study on the welding quality in the porthole die extrusion process of aluminum alloy profiles, Procedia Eng., 2017; 207: 401–406, https://doi.org/10.1016/j.proeng.2017.10.795
35. Leśniak D., Wassermann A., Dziki M., Zaborowski K., and Jurczak H., Susceptibility for Extrusion Welding of AlMg Alloys, Arch. Civ. Mech. Eng., 2019; 19(1): 20–31, https://doi.org/10.1016/j.acme.2018.08.005